




ARTICLE

Tumors with TSC mutations are sensitive to CDK7 inhibition through NRF2 and glutathione depletion

Mahsa Zarei^{1,2*}, Heng Du^{1*}, Amin H. Nassar¹ , Rachel E. Yan¹ , Krinio Giannikou¹, Sneha H. Johnson², Hilaire C. Lam³, Elizabeth P. Henske³, Yubao Wang⁴, Tinghu Zhang^{4,5}, John Asara⁶, and David J. Kwiatkowski¹ 

Tuberous sclerosis complex (TSC) is characterized by tumor development in the brain, heart, kidney, and lungs. In TSC tumors, loss of the TSC1/TSC2 protein complex leads to activation of mTORC1 with downstream effects on anabolism and cell growth. Because mTORC1 activation enhances mRNA transcription, we hypothesized that aberrant mTORC1 activation might confer TSC-null cell dependence on transcriptional regulation. We demonstrate that TSC1- or TSC2-null cells, in contrast to their wild-type counterparts, are sensitive to pharmacological inhibition of CDK7. Mechanistic studies revealed that CDK7 inhibition markedly reduces glutathione levels and increases reactive oxygen species due to reduced expression of NRF2 and glutathione biosynthesis genes. Treatment of both *Tsc2*^{+/-} mice and a TSC1-null bladder cancer xenograft model with a CDK7 inhibitor showed marked reduction in tumor volume and absence of regrowth in the xenograft model. These results suggest that CDK7 inhibition is a promising therapeutic approach for treatment of TSC-associated tumors and cancers with mutations in either *TSC1* or *TSC2*.

Introduction

Tuberous sclerosis complex (TSC) is an autosomal dominant tumor predisposition syndrome characterized by seizures, autism, and tumors of the brain (subependymal giant cell astrocytoma), heart (rhabdomyoma), kidney (angiomyolipoma), skin (angiofibroma), and lungs (lymphangiomyomatosis [LAM]; Crino et al., 2006; Henske et al., 2016). TSC is caused by germline loss-of-function mutations in either *TSC1* or *TSC2* (European Chromosome 16 Tuberous Sclerosis Consortium, 1993; van Slegtenhorst et al., 1997), which encode the proteins hamartin (TSC1) and tuberlin (TSC2), respectively. Hamartin, tuberlin, and TBCID7 form the TSC protein complex, which negatively regulates the activity of the mechanistic target of rapamycin complex 1 (mTORC1) via the small GTPase Rheb (Dibble et al., 2012). mTORC1 consists of the core constituent mTOR (product of the *MTOR* gene) and several regulatory proteins and phosphorylates multiple downstream proteins to promote protein, nucleotide, and lipid biosynthesis as well as anabolism and cell growth, while limiting autophagy (Hara et al., 1998; Yecies et al., 2011; Ben-Sahra et al., 2013, 2016; Zhang et al., 2014).

Clinical trials have demonstrated the benefit of mTORC1 inhibitors for treatment of multiple tumor types seen in TSC, as

well as sporadic renal angiomyolipoma and LAM (Franz et al., 2006, 2013; Bissler et al., 2008; Krueger et al., 2010; McCormack et al., 2011). For example, rapamycin (sirolimus), which inhibits mTORC1 by binding FKBP12, has been shown to slow loss of lung function in LAM and decrease the size of TSC-associated angiomyolipoma (Bissler et al., 2008; McCormack et al., 2011). Everolimus, a rapamycin analogue (“rapalog”), also causes reduction in TSC-associated tumor size and is Food and Drug Administration–approved for the treatment of angiomyolipoma and subependymal giant cell astrocytoma (Krueger et al., 2010; Franz et al., 2013). In vitro studies have shown that rapalogs have a predominantly cytostatic effect on cells with loss of either TSC1 or TSC2, hereafter denoted TSC-deficient cells. In addition, TSC-associated tumors regrow and LAM lung function declines when rapalog therapy is discontinued (Franz et al., 2006; Bissler et al., 2008; McCormack et al., 2011). Therefore, continuous rapalog therapy appears to be necessary in both adults and children with TSC-associated tumors to maintain tumor growth control. Both short-term and long-term toxicity from rapalogs has led to recognition of a critical need for better, more effective therapies for TSC-associated neoplasms.

¹Cancer Genetics Laboratory, Pulmonary and Critical Care Medicine, Department of Medicine, Brigham and Women’s Hospital and Harvard Medical School, Boston, MA; ²Department of Veterinary Physiology and Pharmacology, College of Veterinary Medicine and Biomedical Sciences, Texas A&M University, College Station, TX; ³Pulmonary and Critical Care Medicine, Department of Medicine, Brigham and Women’s Hospital and Harvard Medical School, Boston, MA; ⁴Department of Cancer Biology, Dana-Farber Cancer Institute, Boston, MA; ⁵Department of Biological Chemistry and Molecular Pharmacology, Harvard Medical School, Boston, MA; ⁶Division of Signal Transduction, Department of Medicine, Beth Israel Deaconess Medical Center, Harvard Medical School, Boston, MA.

*M. Zarei and H. Du contributed equally to this paper; Correspondence to David J. Kwiatkowski: dk@rics.bwh.harvard.edu.

© 2019 Zarei et al. This article is distributed under the terms of an Attribution–Noncommercial–Share Alike–No Mirror Sites license for the first six months after the publication date (see <http://www.rupress.org/terms/>). After six months it is available under a Creative Commons License (Attribution–Noncommercial–Share Alike 4.0 International license, as described at <https://creativecommons.org/licenses/by-nc-sa/4.0/>).

Activated mTORC1 has two primary downstream targets, 4E-BP1 and S6 kinase, which have multiple downstream effects including the promotion of protein biosynthesis (Hara et al., 1998). Furthermore, mTORC1 has major effects on transcription, through phosphorylation and activation of STAT3 (Yokogami et al., 2000; Onda et al., 2002), activation and nuclear accumulation of SREBP1 (Düvel et al., 2010; Li et al., 2010; Wang et al., 2011; Yecies et al., 2011), activation of peroxisome proliferator-activated receptor γ (Kim and Chen, 2004), activation of HIF1 α (Brugarolas et al., 2003; El-Hashemite et al., 2003), and inhibition of transcription factor EB (Settembre et al., 2012).

TFIIF is a 10-subunit protein complex that is highly ancestrally conserved (including yeast) and regulates RNA polymerase II (Pol II) transcription (Rimel and Taatjes, 2018). Cyclin-dependent kinase 7 (CDK7) is a core component of TFIIF and is also part of a dissociable three-subunit kinase module (consisting of MAT1, Cyclin-H, and CDK7) known as the CDK-activating kinase complex. CDK7 phosphorylates Ser5 and Ser7 of a heptapeptide repeat in RNA Pol II in a dynamic, tightly regulated manner to regulate transcription (Akhtar et al., 2009; Larochelle et al., 2012; Zhou et al., 2012). Recently, a covalent inhibitor of CDK7, THZ1, was discovered, and studies have suggested that CDK7 is a rational therapeutic target in a number of cancer types (Chipumuro et al., 2014; Christensen et al., 2014; Kwiatkowski et al., 2014; Wang et al., 2015; Zhang et al., 2017). These studies also showed that THZ1 inhibition of CDK7 led to transcriptional effects on core transcription factors that were highly marked by acetylation at histone 3 lysine 27 (H3K27ac), so-called “super-enhancers,” and that this appeared to be an important mechanism for induction of cell death (Chipumuro et al., 2014; Christensen et al., 2014; Kwiatkowski et al., 2014; Wang et al., 2015; Zhang et al., 2017).

Since cells and tumors lacking the TSC complex, as well as those with activating mutations in MTOR (Grabiner et al., 2014), have constitutive mTORC1 activation, and this effect has multiple transcriptional as well as translational effects, we hypothesized that TSC-deficient cells might show selective sensitivity to THZ1. Indeed, treatment of TSC-deficient cells with THZ1 led to profound effects on cell metabolism, growth, and survival in comparison to effects in wild-type or intact derivative cells at similar doses. THZ1 treatment led to marked reduction in expression of NRF2 (encoded by NFE2L2) and genes involved in glutathione (GSH) synthesis; marked depletion of GSH; and an increase in ROS levels in TSC-deficient cells, leading to cell death. Importantly, THZ1 treatment led to regression of both xenograft and transgenic TSC-deficient tumor models. Overall, our data suggest that inhibition of transcription-associated kinases such as CDK7 in mTORC1-driven tumors leads to enhanced oxidative stress through reduced expression of NRF2 and downstream genes, and that this may be an effective therapeutic approach for TSC-deficient tumors.

Results

CDK7 inhibition by THZ1 selectively inhibits the growth of TSC-deficient cells

To investigate whether the proliferation of TSC-deficient cells is sensitive to CDK7 inhibition, we treated paired TSC-deficient/

TSC-intact cell lines with increasing concentrations of THZ1. THZ1 showed selective inhibition of proliferation in TSC-deficient cells versus TSC-intact cell lines ($n = 6$ cell line pairs, 4 TSC2-null, 2 TSC1-null, including both addback and native TSC-intact cell lines; Table S1 and Fig. S1 A) in a standard 96-well plate 5-d growth assay (Fig. 1 A). The half-maximal inhibitory concentration (IC₅₀) of the TSC-deficient cell lines was 8–36-fold lower (median IC₅₀ 26.5 nM, range 16–39 nM) versus the corresponding TSC-intact lines (median 475 nM, range 190–660 nM; Fig. S1 B). Phase-contrast imaging demonstrated that THZ1 treatment (30 nM, 72 h) resulted in dramatic cell death in TSC-deficient cells compared with TSC-intact cells (Fig. 1 B). In addition, low-dilution-plating colony formation assays (10 d) showed that there was a marked reduction in colony formation in TSC-deficient cells in 30 nM THZ1, in contrast to control TSC-intact lines (Fig. 1 C). Furthermore, apoptotic cell death was selectively induced by THZ1 treatment of TSC-deficient cells, as assessed by propidium iodide (PI) staining, and production of cleaved caspase 3, again in contrast to TSC-intact cells (Fig. 1, D and E; and Fig. S1, C and D).

To understand the mechanism of the TSC genotype-specific effect of THZ1, we examined whether CDK7 is inhibited equally in TSC-deficient and TSC-intact cells. CDK7 is a member of the CDK-activating kinase complex of the TFIIF transcription initiation complex that plays a critical role in regulation of transcription through phosphorylation of the carboxyl-terminal domain (CTD) of RNA Pol II at multiple sites. TSC-deficient and TSC-intact cell lines displayed a similar dose-responsive reduction in RNA Pol II CTD phosphorylation in response to THZ1 treatment without affecting total RNA Pol II levels (Figs. 1 F and S1, E and F), suggesting that neither differential uptake of THZ1 nor differential inhibition of CDK7 explained the genotype-specific effect. Together, these data indicate that THZ1 inhibits growth and induces cell death in a TSC-dependent manner.

TSC-deficient cells are highly dependent on CDK7 for survival and proliferation

CDK7, and to a lesser extent CDK12/CDK13, is inhibited by THZ1 (Chipumuro et al., 2014; Christensen et al., 2014; Kwiatkowski et al., 2014). Previous studies in other cell systems have demonstrated that KO of CDK7 inhibits cell survival, suggesting that it is the primary target of THZ1 in causing cell death (Wang et al., 2015; Zhang et al., 2017). Here, to confirm that CDK7 is the critical pharmacological target of THZ1 in TSC-deficient cells, we used CRISPR/Cas9 to genetically knock out CDK7 in two TSC1-null cells, HCV.29 and 97.1, and their TSC-intact derivatives. Immunoblot analysis (Fig. 2 A, left two panels) confirmed a marked reduction in CDK7 expression. KO of CDK7 resulted in a marked reduction in growth of both TSC-deficient (Fig. S2 A, 83–86%), and TSC-intact (Fig. S2 A, 58–62%) cell lines. Similarly, CDK7-KO TSC-deficient cell lines showed a near absence of growth in low-dilution-plating colony formation long-term assays, which was much more reduced than was seen for CDK7-KO TSC-intact control lines in this assay (Fig. 2 B, left two panels). We also used shRNA to decrease expression of CDK7 in paired TSC2-null and TSC2-intact MEF cells, which showed a significant reduction in expression of CDK7, with similar major effects

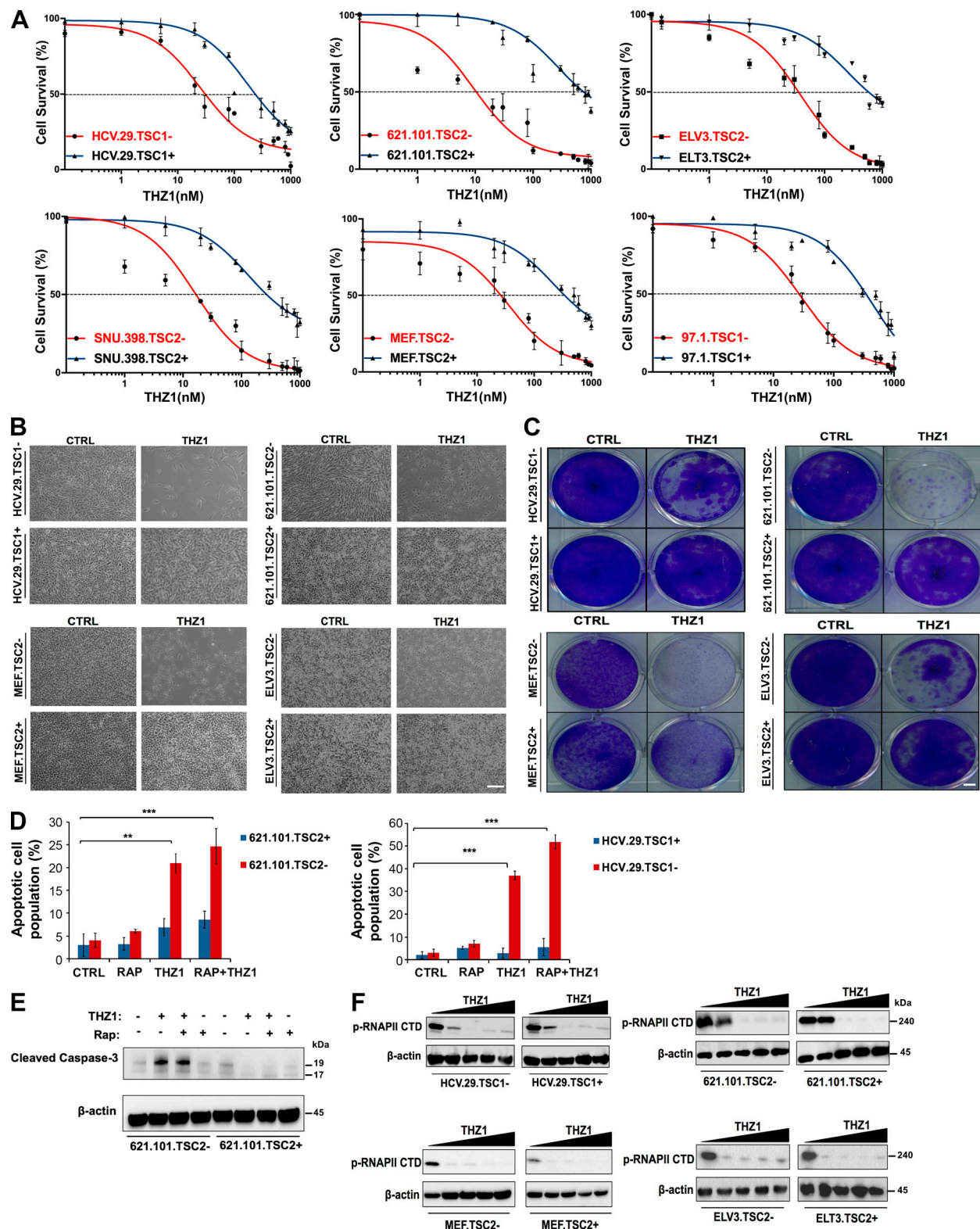


Figure 1. THZ1 inhibition of CDK7 leads to selective growth inhibition and apoptosis of TSC mutant cells. (A) Cell growth curves of TSC-deficient and TSC-intact cell lines treated with the indicated doses of THZ1. Cell number was calculated by measurement of double-stranded DNA (dsDNA) content using PicoGreen after 5 d in 96-well plate assays. Each data point represents the mean of four independent measurements. SEM is indicated. **(B)** Phase-contrast images of cells that were treated with vehicle control or THZ1 (30 nM) for 7 d. Note THZ1-induced death of TSC1 or TSC2 null cells, but not TSC wild-type cells (three independent experiments performed, and ≥ 10 images per field analyzed for each condition). Scale bar, 100 μ m. **(C)** Images of crystal violet-stained dishes that were treated with vehicle control or 30 nM THZ1 for 10 d after plating 1,000 cells per well in a 12-well plate (three independent experiments performed). Scale bar, 2 mm. **(D)** Apoptotic cell fraction was determined after treatment with control (CTRL), rapamycin (RAP; 20 nM), THZ1 (30 nM), or a

combination of both for 72 h. Apoptotic cell death was quantified by Annexin V/PI staining and flow cytometry and is shown as the percentage of cells that were PI positive. Each data point represents the mean \pm SEM of three independent experiments. **, $P < 0.01$; ***, $P < 0.001$. (E) Immunoblot analysis shows that cleaved caspase 3 is increased in total protein lysates from the 621.101 TSC2-deficient cell line treated with THZ1 (30 nM) with or without rapamycin (Rap; 20 nM) for 72 h, but not in the TSC2-intact control line. β -Actin serves as a loading control (three independent experiments performed). (F) Immunoblot analysis shows that THZ1 inhibits RNAPII CTD phosphorylation in both TSC-deficient and TSC-intact cells. Cells were treated with vehicle control (first lane) or increasing concentrations of THZ1 (10, 30, 100, and 1,000 nM) for 4 h before lysates were prepared for immunoblotting (two independent experiments performed).

on both proliferation and growth in low-dilution-plating colony formation assays (Fig. 2, A and B, right panels). Similar results were seen in the TSC2-null 621.101 cell line, using siRNA to CDK7 (Fig. S2 B). To investigate the growth properties of CDK7-KO cells in vivo, we injected two CDK7-KO TSC1-null HCV.29 cell lines, generated with different guide RNAs (gRNAs), into the flanks of nude mice and observed near absence of xenograft formation. In contrast, robust xenograft growth occurred in controls, necessitating mouse sacrifice at 51 d after injection (Fig. 2 C). Reduced CDK7 mRNA levels were confirmed in the xenograft tumor nodules of the CDK7-KO cells (Fig. S2 C).

Because THZ1 has some inhibitory effects on CDK12 and CDK13 at higher doses (Chipumuro et al., 2014; Kwiatkowski et al., 2014), we also examined whether those kinases contributed to the growth inhibition effect of THZ1. We used CRISPR/Cas9 to knock out each gene individually in the TSC1-null HCV.29 and 97.1 cells. In contrast to knock out of CDK7, CDK12-KO and CDK13-KO derivative lines showed no significant reduction in growth and proliferation in low-dilution-plating colony formation assays (Fig. 2, D and E; and Fig. S2 D). Similarly, siRNA-mediated knockdown of CDK7, but not CDK12 or CDK13 in the TSC2-null 621.101 cell line, had significant effects on cell proliferation (Fig. S2 E).

Furthermore, treatment of either siCDK7 621.101.TSC2⁻ cells or CDK7.KO1 HCV.29.TSC1⁻ cells with THZ1 had little or no additional effect in growth inhibition (Fig. S2 F). Altogether, these data suggest that CDK7 is required for survival and proliferation in general but TSC mutant cells exhibit heightened dependence, so CDK7 is the likely target of THZ1 in causing reduced cell growth and apoptosis of TSC-deficient cells.

THZ1-mediated suppression of GSH levels is required for cell death induction in TSC-deficient cells

To investigate the mechanism by which THZ1 is selectively toxic to TSC-deficient cells, we used liquid chromatography/tandem mass spectrometry (MS/MS)-based metabolomics to profile metabolic changes following THZ1 treatment. After 6 h of 30 nM THZ1 treatment, metabolites from the TSC2-null 621.101 cells changed dramatically, with GSH decreased most (72%) among 259 measured metabolites (Fig. 3, A and B; and Table S2). Similar marked reductions in GSH levels were seen for TSC1-null HCV.29 cells and TSC2-null MEFs (Figs. 3 C and S3 A). We also performed steady-state metabolite analysis in CDK7-KO cells and observed a significant reduction (67%) in GSH levels in HCV.29.TSC1⁻ cells in comparison to control (empty vector; EV), while there was no significant reduction in GSH in HCV.29.TSC1⁺ cells (5% reduction; Fig. S3 B and Table S3). To confirm these results, GSH was measured using a GSH-Glo Assay (Promega) after

knockdown of CDK7 (using two independent siRNAs) in 621.101 TSC2-null cells and their parallel TSC-intact cells (Fig. S3 B). Similar marked reductions in GSH levels were seen for TSC2-null 621.101 (45% reduction) by CDK7 silencing, consistent with the steady-state metabolomic data in TSC1-null cells (Table S3).

As GSH is the major intracellular antioxidant peptide, we examined ROS in these cells. THZ1 treatment caused a marked increase in ROS levels in TSC-deficient cells in comparison to parallel TSC-intact cells (TSC2-null 621.101 cells and TSC1-null HCV.29 cells; Fig. 3 D). Elevated ROS levels were observed in TSC-deficient cells, as expected from previous studies (Fig. S3 C; Finlay et al., 2003, 2005), suggesting that THZ1 treatment further increases elevated ROS to a level causing apoptosis induction and cell death.

To examine whether GSH depletion was the proximate cause of apoptosis in THZ1-treated TSC-deficient cells, we treated cells with GSH monoethyl ester (GSH-MEE), a membrane-permeable derivative of GSH. GSH-MEE cotreatment restored ROS levels to near baseline in THZ1-treated TSC-deficient cells and rescued the viability of TSC-deficient cells treated with THZ1 (Fig. 3, E and F; and Fig. S3, F and G). Importantly, GSH-MEE treatment did not affect the reduction in phospho-RNA Pol II levels induced by THZ1-treatment, indicating that GSH-MEE had no direct effect on THZ1 activity (Fig. S3 H). In addition, we examined the effects of antioxidants on cell death induction by THZ1. N-acetyl cysteine (NAC), a ROS scavenger, restored ROS levels to near control in THZ1-treated TSC-deficient cells (Fig. S3, D and F). Furthermore, NAC treatment significantly reduced cell death seen in TSC-deficient cells in response to THZ1 treatment (Fig. S3, E and G).

To determine the functional consequences of GSH depletion in TSC-deficient cells, we also treated cells with buthionine sulfoximine (BSO), an inhibitor of γ -glutamylcysteine synthetase, which leads to reduced GSH levels. Treatment of TSC-deficient cells with BSO showed a dose-dependent and genotype-specific reduction in cell survival and a similar genotype-specific increase in ROS (Li et al., 2015; Fig. S3 I). These observations highlight the importance of ongoing GSH synthesis to combat elevated ROS for the survival of TSC-null cells. Overall, these data suggest that GSH depletion is a critical mechanism of THZ1-induced cell death in TSC-null cells.

To confirm that THZ1 was acting on CDK7 to cause these effects on ROS and cell growth, we treated both the HCV.29.TSC1⁻.CDK7 KO cells and the 621.101.TSC2⁻ cells treated with siRNA to CDK7 (two different siRNAs) with THZ1. THZ1 had no additional effect on these CDK7 KO/siRNA cells in terms of ROS levels or cell growth (Figs. S2 F and S3 J), providing further evidence that THZ1 was acting through CDK7.

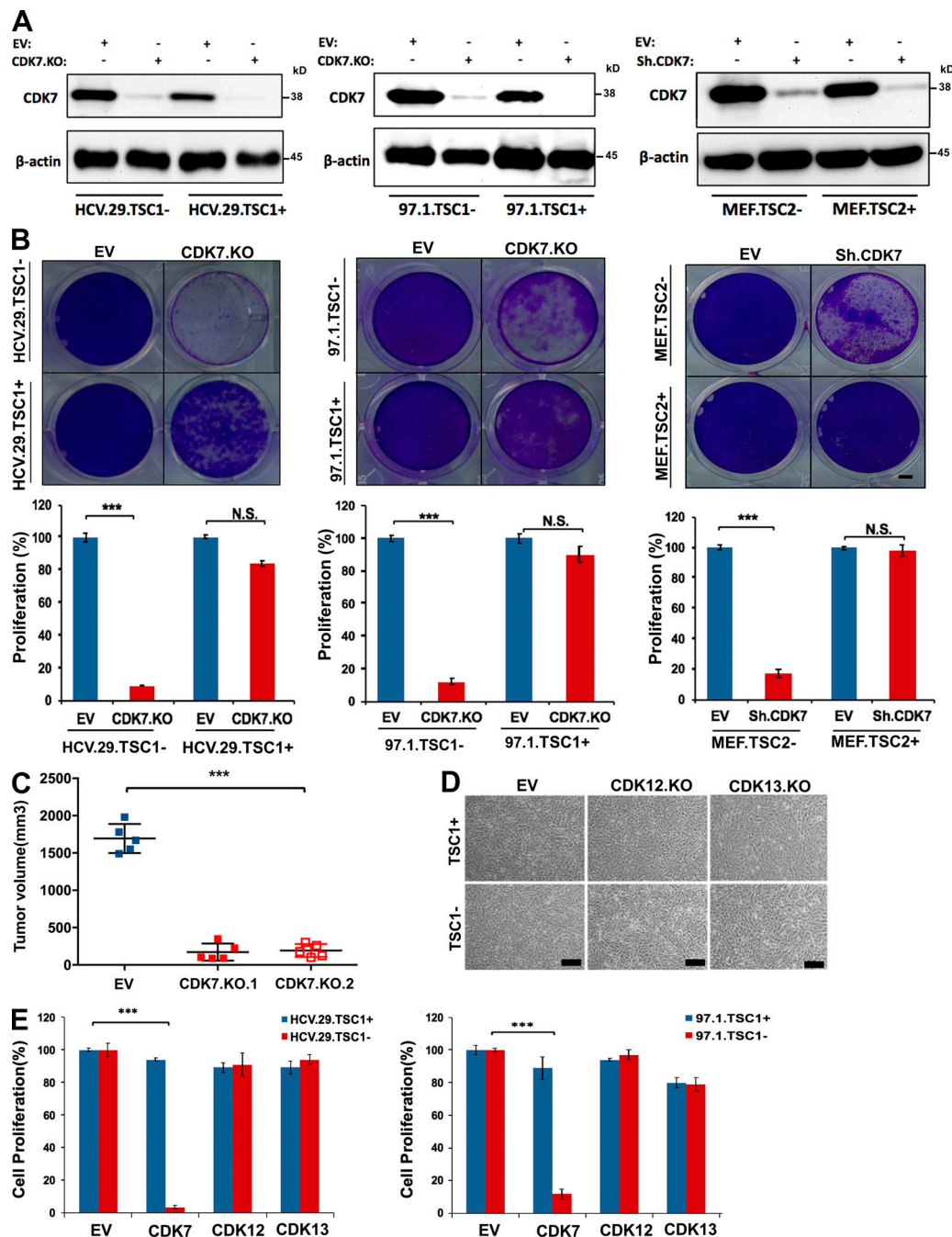


Figure 2. Loss of CDK7 but not CDK12 or CDK13 selectively reduces growth of TSC-deficient cell lines. (A) Immunoblot analysis of cell lines in which CDK7 has been knocked out by either CRISPR/Cas9 (KO, left and middle) or shRNA (right; three independent experiments performed). **(B)** Dilutional clonal growth assays (top) show reduction in colony growth of TSC1-null or TSC2-null cells with CDK7 loss compared with control and TSC-intact cells, crystal violet staining. Quantification of crystal violet staining is shown for three pairs of TSC-null and TSC-intact cell lines. Error bars indicate SEM of triplicate wells from a representative experiment (three independent experiments performed). Scale bar, 2 mm. **(C)** Tumor volume of xenografts derived from HCV.29 cells infected with EV or CDK7.KO.1 or CDK7.KO.2 (two different gRNAs) at 51 d after injection. Cells were infected with lentivirus, selected with puromycin for 2 d, and then harvested for subcutaneous injection. 3 million HCV.29 (viability >94% for all groups, assayed by trypan blue exclusion) were subcutaneously injected into flanks of nude mice. Each data point represents the mean of tumor volume determined by caliper measurements \pm SEM ($n = 5$ per group, two tumors per mouse). **(D)** Phase-contrast images of cells infected with virus encoding EV, CDK.KO.12, and CDK.KO.13. After infection and selection with puromycin (1.5 mg/ml, 96 h), cells were seeded in 6-well plates (5,000 cells per well for HCV.29.TSC1⁻ and HCV.29.TSC1⁺) and imaged with an inverted microscope (three independent experiments performed; ≥ 10 images per field were analyzed for each condition). Scale bar, 200 μ m. **(E)** Quantification of relative cell number by PicoGreen assay in cells with KO of CDK7, CDK12, or CDK13, grown for 5 d. Each data point represents the mean of four independent experiments \pm SEM. N.S., nonsignificant; ***, $P < 0.001$.

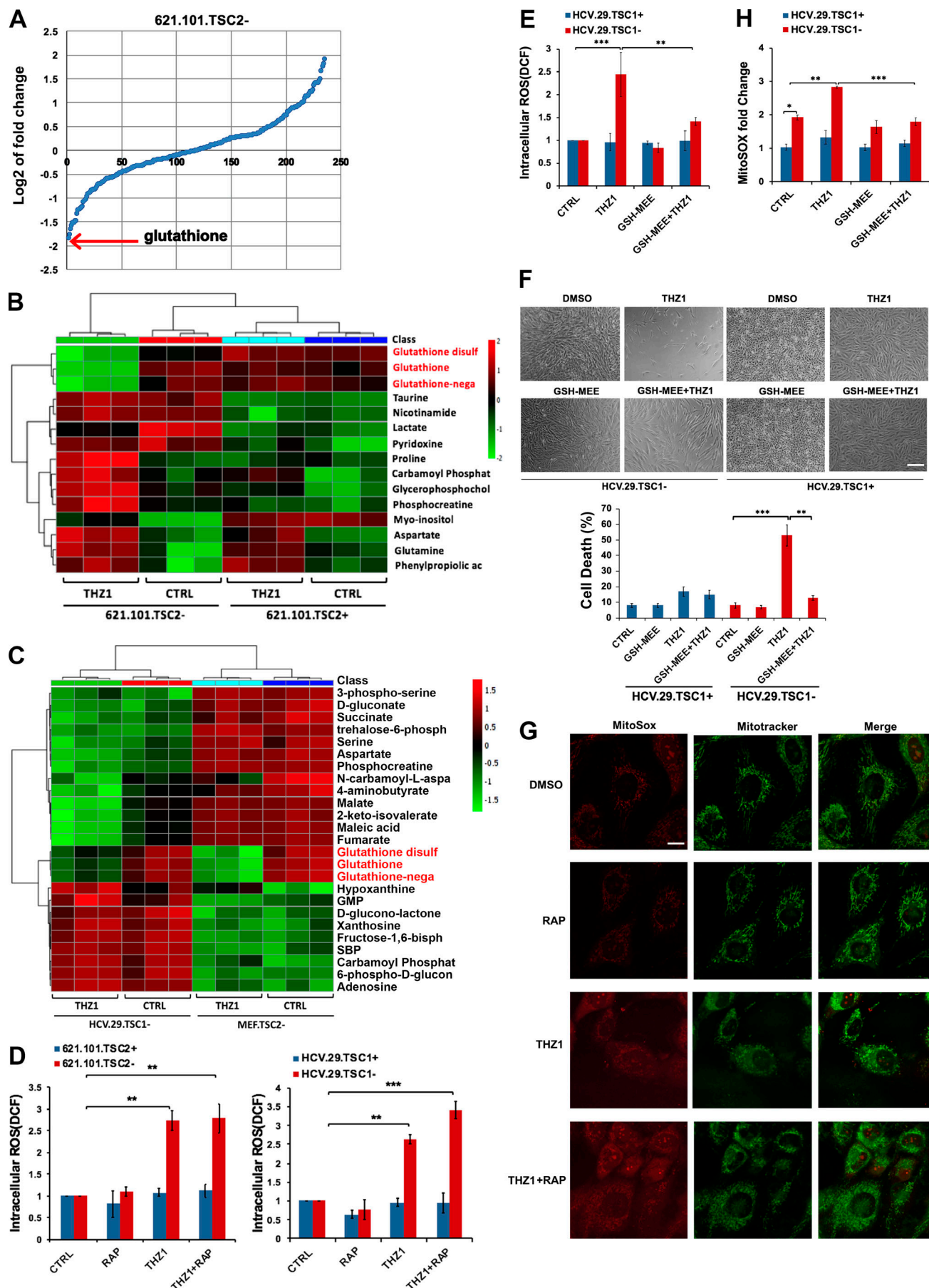


Figure 3. Reduction of GSH and increase in ROS in THZ1-treated TSC-deficient cells. (A) Graph of steady-state metabolite levels in 621.101.TSC2⁻ cells in response to THZ1 at 30 nM for 6 h in comparison to vehicle control. The graph shows the log2 fold change for each metabolite. Arrow indicates GSH. *n* = 3 independent samples. (B) Heat map showing the top 15 metabolites with greatest change in 621.101.TSC2⁻ cells, with comparison to control (CTRL) and similarly treated 621.101.TSC2⁻ intact cells (*n* = 3 samples). The scale is log twofold-change. (C) Heat map showing the top 25 metabolites with greatest change in HCV.29.TSC1⁻ and MEF.TSC2⁻ cells treated with THZ1 at 30 nM for 6 h (*n* = 3 independent samples) versus control (*n* = 3 independent samples). (D) Normalized ROS levels in TSC-deficient and TSC-intact cells treated with control, rapamycin (RAP; 20 nM), THZ1 (30 nM), or the combination for 48 h. Each data point represents the mean ± SEM of three independent experiments. Measured using DCFDA. (E) Normalized ROS levels in TSC-deficient and TSC-intact cells treated with control, THZ1 (30 nM), GSH-MEE (2 mM), or the combination for 48 h. Each data point represents the mean ± SEM of three independent experiments. Measured using DCFDA. (F) Rescue of THZ1-induced cell death by GSH-MEE. HCV.29.TSC1⁻ and HCV.29.TSC1⁺ cells were treated with DMSO (vehicle), THZ1 (30 nM), GSH-MEE (2 mM), or the combination for 48 h. Phase-contrast images are at top. Cell death (%) is shown at bottom for these treatments, measured by Trypan blue staining. Each data point represents the mean ± SEM of three independent experiments. Scale bar, 100 μm. (G) Confocal microscope images of HCV.29.TSC1⁻ cells showing localization of ROS, by staining with MitoSOX (red, 5 μM) and Mitotracker Green (200 nM) in cells treated with DMSO (vehicle), RAP (20 nM), THZ1 (30 nM), or the combination (two independent experiments performed; ≥10 images per slide were analyzed for each condition. Scale bar, 10 μm. (H) Mitochondrial-specific ROS levels were determined by measuring MitoSOX Red fluorescence in HCV.29.TSC1⁻ and HCV.29.TSC1⁺ cells treated with control, THZ1 (30 nM), GSH-MEE (2 mM), or the combination for 48 h. Each data point represents the mean ± SEM of three independent experiments. *, *P* < 0.05; **, *P* < 0.01; ***, *P* < 0.001.

THZ1 induces TSC-dependent cell death via induction of mitochondrial ROS (mtROS)

ROS generation occurs in multiple intracellular sites, including the cytosol, peroxisomes, plasma membrane, and endoplasmic reticulum. However, the majority of ROS are produced in the mitochondria when electrons escape from the mitochondrial respiratory chain and react with molecular oxygen (Trachootham et al., 2009; Venditti et al., 2013). To examine the intracellular localization of the elevated ROS generated in response to THZ1, TSC-deficient cells were treated with THZ1 for 16 h and stained with the mitochondrial O₂⁻ indicator MitoSOX Red. MitoSOX Red is nonfluorescent until oxidized by O₂⁻, and an increase in the fluorescence of MitoSOX Red indicates oxidation by mitochondrial O₂⁻. The samples were counterstained with MitoTracker Green, which localizes to mitochondria regardless of mitochondrial membrane potential, and were then examined by confocal microscopy and quantitatively by plate reader. THZ1 treatment of TSC-deficient cells caused an increase in mtROS compared with DMSO (Fig. 3, G and H). Interestingly, the combination of rapamycin with THZ1 treatment showed a further increase in mtROS levels (Fig. 3 G). Therefore, we conclude that THZ1 induces an increase in mtROS in TSC-deficient cells, and that, either by itself or in combination with a global increase in ROS, leads to TSC-dependent cell death.

THZ1 treatment of TSC-deficient cells leads to major reductions in expression of GSH biosynthesis genes

Given the critical role of CDK7 in transcription through phosphorylation of the RNA Pol II CTD (Drapkin et al., 1996; Akhtar et al., 2009; Glover-Cutter et al., 2009; Kwiatkowski et al., 2014), we expected that THZ1 had major effects on gene transcription. Previous studies with small cell lung cancer, triple-negative breast cancer, ovarian cancer, and other cancer cell types have shown that THZ1 treatment can cause selective loss of cancer-specific oncogene expression through both epigenetic silencing and transcriptional inhibition, leading to tumor cell death (Chipumuro et al., 2014; Christensen et al., 2014; Kwiatkowski et al., 2014; Wang et al., 2015; Zhang et al., 2017).

To examine global gene expression effects in TSC-deficient and TSC wild-type cells, we performed RNA sequencing (RNA-seq) on TSC1-null HCV.29 cells and TSC1-intact HCV.29 cells

treated with 30 and 100 nM THZ1 for 6 h (Table S4). Many genes showed marked changes in expression in comparison with control untreated cells. Furthermore, 1,128 genes showed more than fivefold lower expression in 30 nM THZ1-treated TSC1-null HCV.29 cells compared with 30 nM THZ1-treated TSC1-intact HCV.29 cells (Fig. 4 A). In contrast, 90% of those genes showed similar levels (<1.5-fold up or down) in the two cell lines untreated (Table S4). Pathway enrichment analysis of differentially expressed genes in THZ1-treated TSC1-null cells compared with TSC1-intact cells showed that they were most significantly enriched for the pathway Oxidative Stress Induced Gene Expression Via Nrf2 (*P* = 0.0004, false discovery rate *q* = 0.05; Table S5), using Enrichr and Biocarta analysis. Given our observations on reduction in GSH levels, we focused on levels of NFE2L2, the master transcription factor that regulates multiple key genes for antioxidant defense known to play a vital role in protecting cells from ROS (Tonelli et al., 2018). NFE2L2 levels were reduced by 94% in the 30 nM THZ1-treated HCV.29 TSC1⁻ cell line in comparison to untreated cells, in contrast to a 60% reduction in the THZ1-treated HCV.29 TSC1-intact cell line compared with untreated cells (Table S6). Hence, NFE2L2 levels were reduced in the 30 nM THZ1-treated HCV.29 TSC1⁻ cell line by 87% in comparison to the 30 nM THZ1-treated HCV.29 TSC1-intact cell line (Fig. 4 A and Table S4).

Key genes regulated by NRF2 include GSH synthetic enzymes to enhance levels of GSH (Harvey et al., 2009; Hayes and Dinkova-Kostova, 2014). GSH is synthesized by the consecutive action of two enzymes, glutamate-cysteine ligase and GSH synthetase. Glutamate-cysteine ligase is composed of the glutamate-cysteine ligase catalytic subunit (GCLC) and the glutamate-cysteine ligase modifier subunit (GCLM) and is the rate-limiting enzyme for GSH synthesis. GSH exists in both reduced (GSH) and oxidized (GSH disulfide; GSSG) states, and GSH is oxidized into GSSG by ROS. GSH is regenerated from GSSG by the enzyme GSH reductase (GSR).

Levels of NRF2-regulated GSH biosynthetic enzyme genes GSR, GCLC, and GCLM were reduced by 95, 91, and 89% in the HCV.29 TSC1⁻ cell line following 30 nM THZ1 treatment, while reductions of 53, 48, and 57% were seen in the THZ1-treated HCV.29 TSC1-intact cell line (Table S6). Considering 10 antioxidant GSH-related genes known to be positively regulated by NRF2 (Harvey et al.,

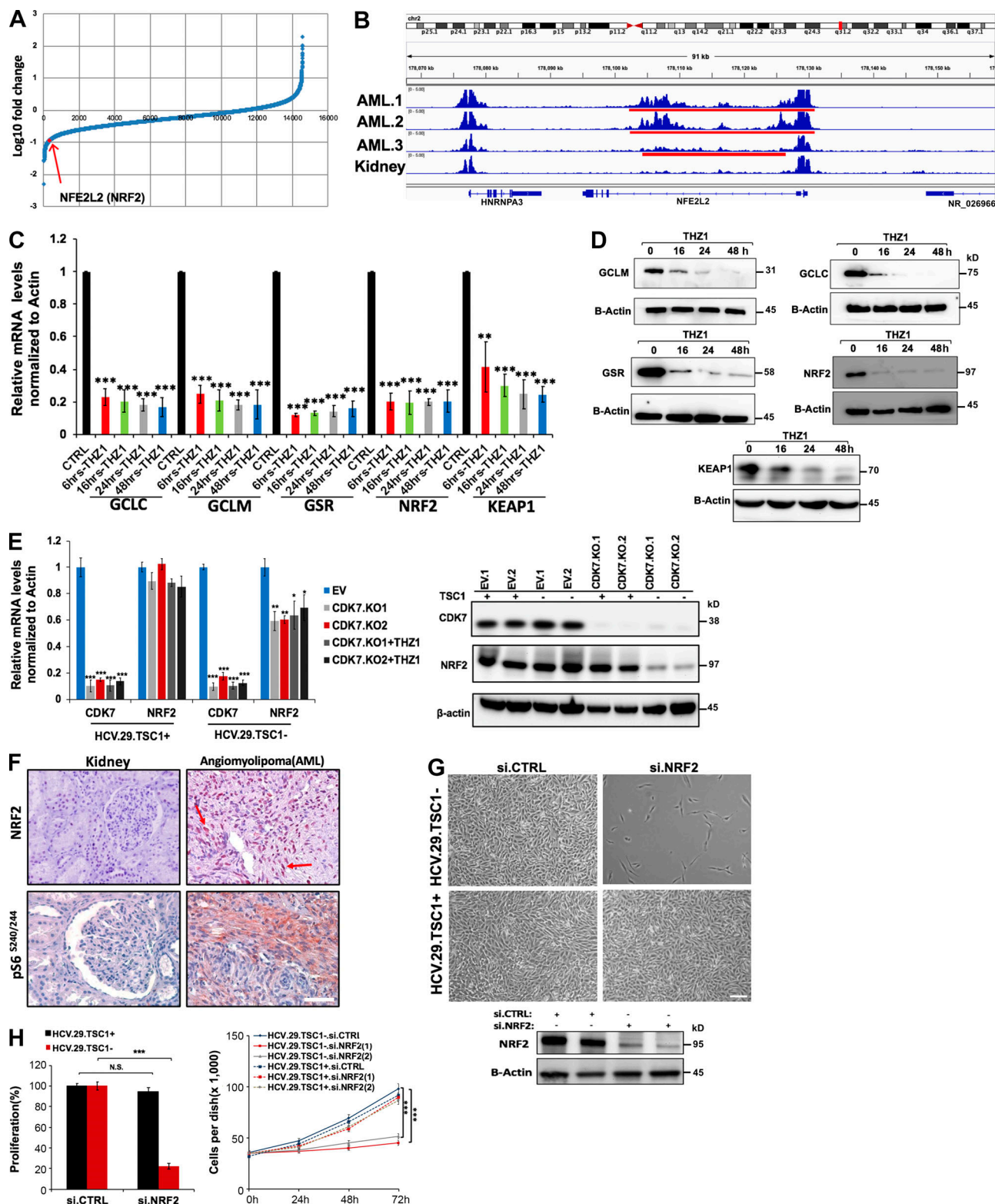


Figure 4. NFE2L2 (NRF2) and GSH synthetic genes are reduced in expression in TSC-deficient cells in response to THZ1 treatment. (A) The ratio between mRNA levels assessed by RNA-seq for 30 nM THZ1-treated HCV.29.TSC1⁻ cells in comparison to 30 nM THZ1-treated HCV.29.TSC1-intact cells, each treated for 6 h. The majority of transcripts are reduced in expression; red arrow (dot) indicates NFE2L2 (NRF2), which is reduced by 87%. Average of two independent samples assessed by RNA-seq. **(B)** H3K27ac ChIP-seq data for three kidney angiomyolipomas demonstrates read depth (bigWig data) in or near NFE2L2. H3K27ac ChIP-seq data from a normal kidney are also shown as control for comparison. All angiomyolipomas had loss of TSC2. A superenhancer region identified by ROSE is highlighted in red. **(C)** Relative mRNA expression of the indicated genes in HCV.29.TSC1⁻ cells treated with vehicle (CTRL) or 30 nM THZ1 for the indicated periods of time. Gene expression is normalized to actin. Each data point represents the mean ± SEM of three independent experiments. **(D)** Immunoblot analysis of NRF2, KEAP1, and GSH synthetic enzymes in HCV.29.TSC1⁻ cells treated with 30 nM THZ1 for varying periods of time (hours).

β -Actin serves as a loading control (two independent experiments performed). **(E)** Q-RT-PCR analysis of CDK7 expression and NRF2 after CDK7 KO (CDK7.KO) treated with or without THZ1 compared with control (EV) in HCV.29.TSC1⁻ and HCV.29.TSC1⁺ (top). Immunoblot analysis of lysates is shown at bottom. Each data point represents the mean \pm SEM of three independent experiments. Note that data for two different gRNAs is shown, and that THZ1 has no effect on NRF2 levels. **(F)** NRF2 and pS6^{S240/244}, assessed by IHC, is shown in normal kidney and an angiomyolipoma that has loss of TSC2 (by sequencing). Nuclear localization of NRF2 is indicated by arrows. Representative image taken from one of three patient angiomyolipoma slides; at least eight images per slide were analyzed for each condition (Table S7). Scale bar, 50 μ m. **(G)** Phase-contrast images (left) of HCV.29.TSC1⁻ and HCV.29.TSC1-intact cells transfected with control siRNA (si.CTRL) or siRNA against NRF2 (si.NRF2) after 3 d (top). Two independent experiments were performed; ≥ 10 images per field were analyzed for each condition. Scale bar, 100 μ m. Immunoblot analysis of lysates is shown at bottom (two independent experiments performed). **(H)** PicoGreen cell number assay at 5 d in HCV.29.TSC1⁻ and HCV.29.TSC1⁺ cells after NRF2 silencing, along with siRNA controls (top). Cell growth (Trypan blue assays, 72 h) of HCV.29 after NRF2 silencing compared with control (EV) for indicated time points (bottom). Each data point represents the mean \pm SEM of three independent experiments. N.S., nonsignificant; *, $P < 0.05$; **, $P < 0.01$; ***, $P < 0.001$.

2009; Hayes and Dinkova-Kostova, 2014), the median reduction in expression levels was 86% in the THZ1-treated HCV.29 TSC1⁻ cell line, while it was 55% for the THZ1-treated HCV.29 TSC1-intact cell line (Table S6). These observations suggest that THZ1 inhibition of CDK7 leads to reduction in expression of NFE2L2 and its target GSH synthetic genes, leading to reduction of GSH and elevated ROS selectively in TSC-null cells.

As above, previous reports have shown that superenhancer-associated genes are particularly sensitive to THZ1 inhibition of CDK7 (Lovén et al., 2013; Chipumuro et al., 2014; Kwiatkowski et al., 2014). We examined H3K27ac marks in human angiomyolipoma, the most common and serious TSC-related tumor, and found that NFE2L2 was highly marked, denoted a superenhancer by rank ordering of superenhancers (ROSE) analysis in 3 of 10 tumors examined (Fig. 4 B).

To confirm and extend these observations, we performed quantitative RT-PCR (Q-RT-PCR) experiments and immunoblotting to assess mRNA and protein levels for NRF2-regulated GSH biosynthetic enzyme genes in both HCV.29 TSC1⁻ cells and 621.101 TSC2⁻ cells (Figs. 4, C and D; and Fig. S4 B). NRF2, GCLM, GCLC, and GSR mRNA and protein levels showed a rapid decline from untreated to 48 h of treatment with 30 nM THZ1, which was more rapid in the HCV.29 TSC1⁻ cell line, such that protein levels were extremely low at 48 h of drug for each cell line. Interestingly, KEAP1 mRNA and protein levels were also markedly reduced in these cell lines (Fig. 4, C and D; and Fig. S4 B), suggesting that accelerated degradation of NRF2 by KEAP1 did not contribute to the reduction in NRF2 levels seen in these TSC-null cells.

To confirm that the mechanism of NRF2 depletion by THZ1 was due to CDK7 inhibition, we examined effects of knockdown/KO of CDK7 in TSC-deficient and TSC-intact cells. Both NRF2 mRNA and protein levels were markedly reduced with knockdown/KO of CDK7 in HCV.29.TSC1⁻ and 621.101.TSC2⁻ cells compared with the control lines with similar knockdown/KO (Figs. 4 E and S4 C, top and bottom panels).

To examine the potential relevance of these observations in vivo, we examined kidney angiomyolipoma. This tumor showed relatively high nuclear expression of NRF2 and phospho-S6 (mTORC1 activation marker), in comparison to normal kidney by immunohistochemistry (IHC; Fig. 4 F and Table S7, $n = 3$; two of two with material sufficient for genetic analysis had inactivating TSC2 mutations), suggesting that high NRF2 expression and activity is a consistent response to TSC complex loss in vivo as well as in vitro.

To confirm that TSC-deficient cells and not TSC-intact cells were dependent on NFE2L2 expression, we used siRNA to knock down NRF2 and found that NRF2 siRNA led to reduced levels of NRF2 and marked reduction in the survival of HCV.29.TSC1⁻ (~75%) and 621.101.TSC2⁻ (~80%) cells in contrast to TSC-intact cells (Fig. 4, G and H; and Fig. S4 F); a major reduction in GSH levels; an increase in ROS levels by ~65%; and reduction of expression of both NRF2 and GSH synthesis enzyme genes (GCLM, GCLC, GSR, and G6PD; Fig. S4, D and E), indicating that TSC-deficient cells are indeed more dependent on NRF2 activity than wild-type cells.

We also used a small-molecule inhibitor of NRF2, ML385 (Singh et al., 2016), to examine the dependence of TSC-deficient cells on NRF2 expression. We observed a dose-dependent reduction in NRF2 protein levels (Fig. S4 H) and its target genes' mRNA levels (Fig. S4 K). In addition, we observed a significant reduction in GSH levels and a modest increase in ROS levels (not significant) after treatment with ML385, consistent with previous reports (Singh et al., 2016; Fig. S4, I and J). Two different TSC-deficient cell lines showed a differential sensitivity to ML385 in comparison to TSC-intact controls, with a four- to sixfold difference in IC₅₀ (Fig. S4 L). Thus, these data provide further evidence that TSC complex loss leads to mTORC1 activation, leading to high ROS levels, and dependence on NRF2-driven GSH biosynthetic gene expression to enable survival and growth.

Therefore, in aggregate, these data suggest that overproduction of ROS by TSC-deficient cells leads to dependence on NRF2 expression for GSH production to counterbalance high ROS levels. CDK7 inhibition in TSC-deficient cells leads to a marked decrease in NRF2 through both epigenetic and transcriptional mechanisms, leading to high ROS levels and cell death.

THZ1 has antitumor efficacy in both genetic and xenograft tumor models of TSC

We next examined whether THZ1 treatment can be effective for inhibition of TSC-related tumor growth in vivo. Tsc2^{+/-} A/J strain mice develop kidney cystadenomas by 4 mo of age and provide a native in vivo model that is genetically identical to human TSC patients that is driven by spontaneous second-hit events that lead to complete loss of Tsc2 expression and mTORC1 activation (Woodrum et al., 2010; Auricchio et al., 2012; Guo and Kwiatkowski, 2013). Tsc2^{+/-} A/J mice were treated with vehicle, THZ1, or rapamycin for 1 mo beginning

at 5.5 mo of age (Fig. 5 A). THZ1 was administered by i.p. injection of 10 mg/kg twice daily for 29 d (Wang et al., 2015), and rapamycin i.p. at 3 mg/kg three times per wk. The mice tolerated this treatment well, without loss of body weight or other obvious effect (Fig. S5 A). Rapamycin led to a dramatic reduction in tumor volume, by ~99%, as assessed semiquantitatively on H&E-stained sections (Fig. 5, B and C), consistent with what was previously seen (Guo and Kwiatkowski, 2013). THZ1 also showed dramatic effects similar to those of rapamycin, also reducing tumor volume by ~99% (Fig. 5, B and C). Consistent with this major response, there was a prominent difference in tumor histological appearance, with posttreatment kidney lesions consisting of cysts with rare small papillary extensions into the cyst lumen (Fig. 5 D). In contrast, papillary and solid adenoma lesions were seen in the vehicle-treated mice. Ki67 staining, indicative of proliferation, was markedly reduced in the residual lesions seen after either rapamycin or THZ1 (Fig. 5 E). In addition, cystadenoma cells comprising these lesions showed robust expression of NRF2 before, but not after, treatment with THZ1 (Fig. 5 F). Furthermore, THZ1 treatment resulted in a marked reduction in GSH levels (Fig. 5 G, 55%), indicating inhibition of NRF2 expression and GSH depletion by THZ1 treatment.

To validate these observations of in vivo efficacy of THZ1 for treatment of tumors with TSC complex loss, we used the TSC1-null HCV.29 cell line as a xenograft model. Xenografts were generated by standard subcutaneous injection, and mice were then randomized to treatment with vehicle, THZ1 (10 mg/kg i.p. twice daily), rapamycin (3 mg/kg i.p. 3 d per wk), or both drugs. Treatment was initiated 4 wk after flank injection of HCV.29 cells, when tumors first became palpable and measurable (Fig. 6 A). No effect on body weight or other evidence of toxicity was observed (Fig. S5 B).

Both THZ1 alone and the combination of THZ1 and rapamycin led to a major reduction in the size of the tumor xenografts, with an average volume reduction of 13-fold in comparison to the vehicle and rapamycin-only treated groups after 4 wk of treatment (Fig. 6 A). Ki67 staining showed that all three treatments caused a reduction in proliferation rate, although this was more robust for both THZ1 and the combination treatment in comparison to rapamycin alone (Fig. 6 B). In cohorts of treated HCV.29 xenograft mice, treatments were discontinued after 1 mo, and mice were observed without further intervention. Mice treated with rapamycin alone showed progressive tumor growth over the following 2 mo. In contrast, mice treated with either THZ1 alone or THZ1 and rapamycin showed no recurrence of subcutaneous tumors during that interval (Fig. 6 C). In addition, both THZ1 alone and the combination treatment led to significantly higher levels of cell death in comparison to rapamycin alone or vehicle, as indicated by terminal deoxynucleotidyl transferase-mediated dUTP nick-end labeling (TUNEL) staining (Fig. 6 D).

Taken together, these results indicate that THZ1 inhibition of CDK7 has marked effects in vivo, inhibiting growth of both TSC1-null and TSC2-null cells and causing sustained tumor size reduction, likely through elevation of ROS and stimulation of apoptotic cell death (Fig. 6 E).

Discussion

TSC is often a devastating clinical disorder in which affected children and adults are at high risk for several unusual tumors, including brain subependymal giant cell astrocytomas, cardiac rhabdomyomas, kidney and liver angiomyolipomas, facial angiofibromas and ungual fibromas, and pulmonary LAM. Collectively, these tumors have an incidence of near 100% in TSC individuals and require surgical or medical intervention in more than one quarter (Henske et al., 2016).

A major breakthrough in our understanding of the pathogenesis of TSC occurred when the role of the TSC protein complex in the regulation of the rheb GTPase, and of mTORC1, was discovered (Inoki et al., 2003). This led to in vitro and in vivo animal model studies proving the benefit of rapalog therapy and rapid introduction of these therapies into TSC patients (Franz et al., 2006). Although efficacious in many patients, rapalog therapy has not been shown to exhibit universal benefit in those with TSC. In addition, although tumor regression is seen in response to rapalogs in multiple types of TSC-associated tumors, the degree of response is modest in most cases, rarely meeting RECIST (Response Evaluation Criteria in Solid Tumours) v1.1 criteria for response (Bissler et al., 2013; Franz et al., 2013). In addition, multiple side effects of rapalog therapy are common, including aphthous stomatitis, hypercholesterolemia, acne, and nasopharyngitis, leading to treatment discontinuation in 10–20% of patients (Bissler et al., 2017; Davies et al., 2017). Furthermore, rapalog therapy withdrawal in patients with TSC-associated tumors typically leads to rapid regrowth of such tumors (Franz et al., 2006; Bissler et al., 2013). This limitation necessitates continued administration of rapalog therapy in patients with TSC. Long-term effects of this practice in children and adults are unknown, as this clinical experiment of long-duration rapalog therapy has never been performed previously.

Due to these limitations to rapalog therapy, a search for alternative therapies for tumors with loss of a functional TSC protein complex and constitutive mTORC1 activation goes on, with several recent efforts focused on downstream metabolic consequences of mTORC1 activation (Choo et al., 2010; Düvel et al., 2010; Parkhitko et al., 2014; Valvezan et al., 2017). Here we adopted a different approach and focused on targeting transcriptional effects of mTORC1, given the multiple transcriptional alterations and mechanisms that occur downstream of activated mTORC1 (Yokogami et al., 2000; Onda et al., 2002; Brugarolas et al., 2003; El-Hashemite et al., 2003; Kim and Chen, 2004; Düvel et al., 2010; Li et al., 2010; Wang et al., 2011; Yecies et al., 2011; Settembre et al., 2012).

We found a differential sensitivity to treatment with THZ1, a selective and covalent CDK7 inhibitor, in multiple cell lines with loss of either TSC1 or TSC2, and of different origins, including human, mouse, and rat. The TSC-deficient lines showed enhanced growth inhibition and induction of apoptosis in response to THZ1, due to elevated global and mtROS, and depletion of GSH. RNA and protein studies showed that this was due to marked reduction in expression of NRF2 (*NFE2L2*), as well as its downstream target genes *GCLC*, *GCLM*, and *GSR* that are essential for biosynthesis of GSH. In retrospect, this dependence on NRF2 function to produce GSH in TSC-deficient cells might have been

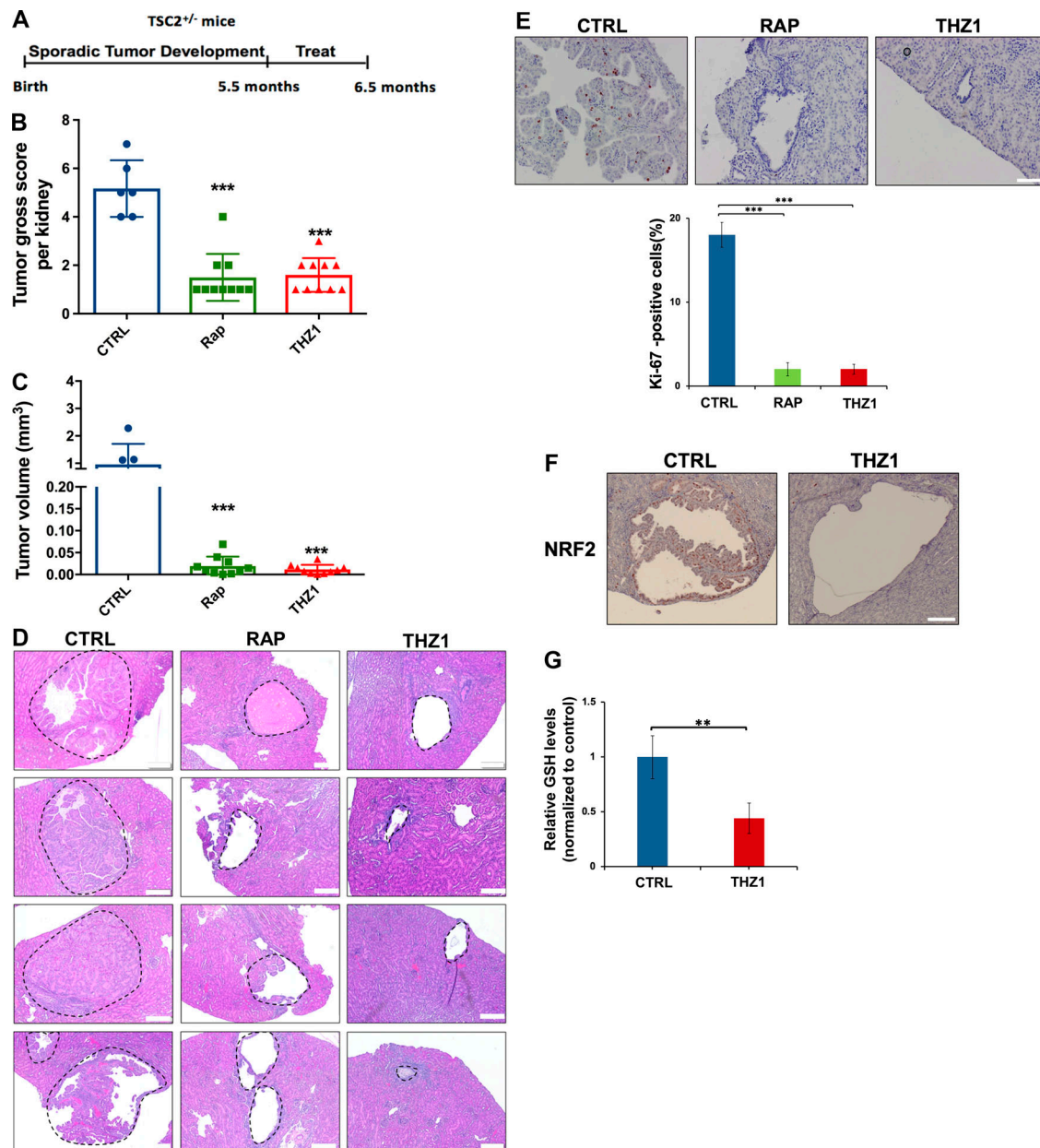


Figure 5. Effects of CDK7 inhibition with THZ1 on kidney tumor development in *Tsc2*^{+/-} mice. (A) Experimental plan. *Tsc2*^{+/-} A/J strain mice were randomized at age 5.5 mo to vehicle (DMSO), THZ1 (10 mg/kg i.p. two times per day), or rapamycin (3 mg/kg i.p. 3 d per wk). They were treated for 1 mo, and then pathology was assessed. (B) Number of tumors per kidney observed by gross inspection for each treatment group. Each data point corresponds to one kidney. (C) Tumor volume per kidney determined by semiquantitative microscopic assessment. Each data point corresponds to one kidney. (D) Renal cystadenoma histology in the treated mice. Representative H&E tumor images are shown for each treatment cohort at 100 \times . Four cystadenomas are shown for vehicle (CTRL), rapamycin (RAP), and THZ1 treatment cohorts, and at least eight images per slide were analyzed for each condition (Table S7). Scale bar, 200 μ m. (E) Ki-67 staining to assess cell proliferation in kidney sections from the treated mice. All images are at 100 \times magnification. Percentage of tumor cells with nuclear immunoreactivity of Ki-67 was scored from six random fields per section ($n = 4$ kidneys per group). Scale bar, 50 μ m. (F) NRF2 expression by IHC in *Tsc2*^{+/-} mouse kidney tumors from control and THZ1-treated mice ($n = 4$ kidneys per group). Scale bar, 50 μ m. (G) Relative GSH content was measured by GSH-Glo assay in kidney lysates from vehicle (CTRL) and THZ1 treatment cohorts ($n = 2$ kidneys per group). Each data point represents the mean \pm SEM with **, $P < 0.01$; ***, $P < 0.001$.

predicted based on multiple studies that identified elevated ROS levels in such cells (Finlay et al., 2005; Chen et al., 2008; Choo et al., 2010). H3K27ac chromatin immunoprecipitation (ChIP) experiments showed that the *NFE2L2* promoter region was highly enriched for histone modification marks in TSC-deficient cells compared with intact controls, indicating the importance of

NRF2 expression in such cells. The sensitivity of NRF2 expression to THZ1 treatment in TSC-deficient cells is reminiscent of earlier findings that THZ1 leads to inhibition of expression of critical core transcription factor genes in other cancer cell types (Chipumuro et al., 2014; Christensen et al., 2014; Kwiatkowski et al., 2014; Wang et al., 2015).

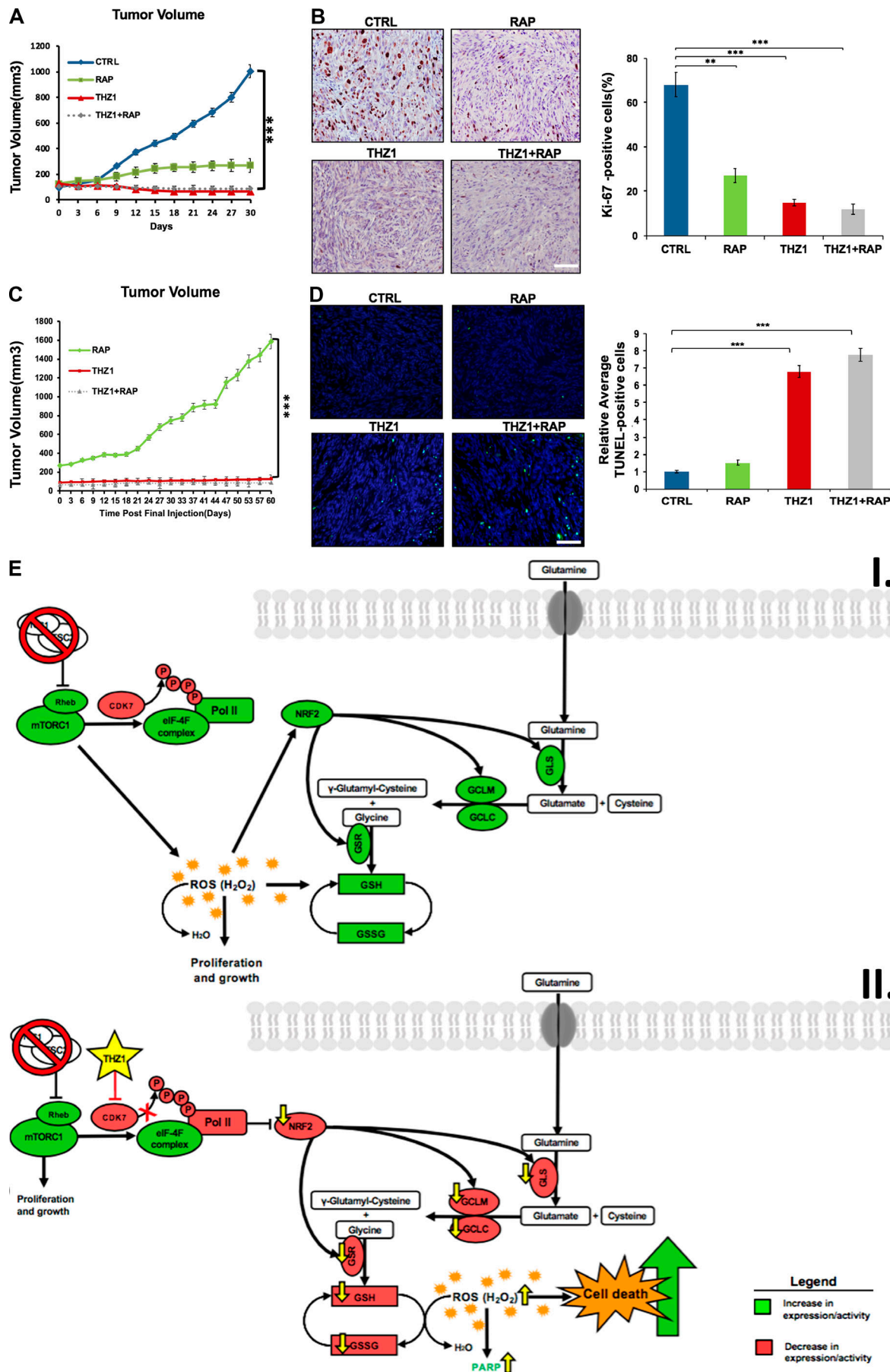


Figure 6. Effects of CDK7 inhibition with THZ1 on tumor xenograft development using TSC1-null HCV.29 cells, and model of effect of CDK7 inhibition. (A) TSC1-null HCV.29 xenograft mice were treated with vehicle (CTRL), rapamycin (RAP; 3 mg/kg i.p. three times per wk), THZ1 (10 mg/kg i.p. two times daily), or combined rapamycin and THZ1, for 30 d, when control tumors reached 100 mm³ in size. Tumor size was assessed every third day using digital calipers (*n* = 5 per group, two tumors per mouse). **(B)** Tumor xenograft cell proliferation was markedly reduced in mice treated with rapamycin, THZ1, or both, in comparison to control, as assessed by nuclear staining using Ki-67. This was quantified by counting four to six random fields per section. Scale bar, 50 μ m. **(C)** Tumor volume of HCV.29.TSC1⁻ xenograft mice treated with rapamycin, THZ1, or the combination in the 60 d following treatment cessation (continuation of A). *n* = 4 tumors per group. **(D)** Apoptotic cell death was increased in tumors from mice treated with THZ1 or combined rapamycin-THZ1, in comparison to vehicle or rapamycin treatment labeled by TUNEL. This was quantified by counting four to six random fields per section. *n* = 4 tumors per group. Scale bar, 50 μ m. **(E)** Diagram showing GSH synthetic pathway and ROS generation in TSC-deficient cells. Top, TSC-deficient cells have hyperactive mTORC1, leading to increased ROS, NRF2 induction, and an increase in transcription of GSH synthetic genes to yield more GSH to buffer the increased ROS. Bottom, THZ1 inhibits transcription by covalently binding to CDK7 and blocking RNA Pol II phosphorylation, leading to marked reduction in NRF2 and downstream gene expression, depletion of GSH stores, and apoptotic cell death. Each data point represents the mean \pm SEM with **, *P* < 0.01; ***, *P* < 0.001.

ROS are known to be increased in many cancer cell types compared with their normal counterparts, which can be due to increased metabolic activity, mitochondrial dysfunction, and/or other oncogenic effects (Liou and Storz, 2010; Chio and Tuveson, 2017; Moloney and Cotter, 2018). A mild increase in ROS can lead to an adaptive survival response, including expression of NRF2 to increase GSH production, whereas a severe increase in ROS can trigger apoptosis. Hence, it has been recognized for some time that cancer cells are potentially vulnerable to treatments that enhance ROS levels and cause cell death (Trachootham et al., 2009; Kim et al., 2016; Chio and Tuveson, 2017; Teppo et al., 2017; Moloney and Cotter, 2018). Several strategies have been employed to induce ROS, including ionizing radiation, inhibition of the ubiquitin-proteasome pathway, and perturbing GSH, glucose, and glutamine metabolism (Gorrini et al., 2013).

Based on the current findings, it is possible that CDK7 inhibition therapy may be broadly effective as a cancer treatment, due to consistent elevation in ROS production in multiple cancer types. Further study is required to assess this possibility. However, homozygous mutations in TSC1 are seen in ~8% of bladder cancer (Robertson et al., 2017) and in TSC1 or TSC2 in ~50% of perivascular epithelioid cell neoplasms (Dickson et al., 2013), and activating mutations in MTOR are seen in ~5% of clear cell renal cell carcinoma (Ricketts et al., 2018). Furthermore, our TSC1-deficient bladder cancer cell line xenograft model showed a sustained and complete response to THZ1 treatment (Fig. 6 A). These results suggest that CDK7 inhibition therapy may be useful for these cancer types and mutations, in addition to TSC-associated neoplasms.

In summary, we have discovered a CDK7-dependent transcriptional addiction to NRF2 in TSC-deficient cells, which when disrupted leads to rapid onset of apoptotic cell death both in vitro and in vivo due to depletion of GSH and high ROS. In both a xenograft and native genetic model of TSC-deficient tumors, we show that THZ1 treatment leads to robust and durable clinical responses. Furthermore, this treatment approach may well be applicable to non-TSC-associated cancers in which there is loss of either TSC1/TSC2 or an activating mutation in MTOR. Since a derivative compound of THZ1, SY-1365, is already in early-phase human clinical trials, assessment of the benefit of this treatment approach should be possible in the near future.

Materials and methods

Cell lines and cell culture

Bladder cancer cell lines transduced with vector control or TSC1 (HCV.29, 97.1; Guo et al., 2013), SNU-398 liver cancer cells with

stable vector or TSC2 intact, angiomyolipoma cells (621.101) with stable vector or TSC2 intact (Yu et al., 2004; Li et al., 2014), ELT-V3/T3 with stable vector or TSC2 intact (Huang et al., 2008), and MEFs, which are native murine embryo fibroblasts genetically engineered to have loss of Tsc2 in one case and to be wild type in the other (Zhang et al., 2003), were maintained in high-glucose DMEM supplemented with 10% FBS and 1% penicillin/streptomycin (Invitrogen). The ELT3-V3/T3 cell medium also contained puromycin at 2 μ g/ml, and the HCV.29 and 97.1 cell medium contained hygromycin at 2 μ g/ml (both from Invitrogen). For packaging virus, HEK293T cells were grown in DMEM with 10% FBS and 1% penicillin/streptomycin. Parental lines and their genetic modifications are summarized in Table S1.

MEFs with stable suppression of CDK7 were generated using lentiviral transduction of shRNAs using a Tet-pLKO-puro backbone plasmid (Addgene; 21915), as described (Wang et al., 2015). The sequences are Scramble (forward [F]: 5'-CCGGGTGGACTCTTGAAAGTACTATCTCGAGATAGTACTTTCAAGAGTCCACTTTTG-3'; reverse [R]: 5'-AATTAAGGAGTGGACTCTTGAAAGTACTATCTCGAGATAGTACTTTCAAGAGTCCAC-3') and CDK7_1 (F: 5'-CCGGGTGACACCATCACACATCAACTCGAGTTGATGTGTGATGGTGCAGCTTTTGG-3'; R: 5'-AATTCAGGAGCTGACACCATCACACATCAACTCGAGTTGATGTGTGATGGTGCAGC-3').

CRISPR/Cas9-mediated KO of CDK7, CDK12, and CDK13 in HCV.29 and 97.1 cells were accomplished using all-in-one lentiviral CRISPR vectors. Plasmids were designed and purchased from Addgene (49535) along with the CRISPR Universal Negative Control plasmid (CRISPR06-1EA) as previously described (Wang et al., 2015). The gRNA sequences are GFP (F: 5'-CACCGGGGAGAGAGCTGTTACCG-3' and R: 5'-AAACCGGTGAACAGCTCCCGCC-3'), CDK7_1 (F: 5'-CACCGGAAGCTGGACTTCTTGGG-3' and R: 5'-AAACCCCAAGGAAGTCCAGCTTCC-3'), CDK7_2 (F: 5'-CACCGATCTCTGGCCTGTAAACGG-3' and R: 5'-AAACCGTTTACAAGGCCAGAGATC-3'), CDK12 (F: 5'-CACCGGGGGAGACAGATCTCCACC-3' and R: 5'-AAACCGGTGGAGATCTGTCTCCCGCC-3'), and CDK13 (F: 5'-CACCGAGGAGCGGCAACAGCAGCG-3' and R: 5'-AAACCGCTGCTGTGGCGCTCCTC-3').

Cell growth assays

Cells were plated in 96-well plates at 10³ cells per well and treated the next day with THZ1 at various concentrations. After 5 d of incubation, cell growth was measured using Quant-it PicoGreen dsDNA assay kit (Invitrogen; Zarei et al., 2017). To estimate cell death, cells were trypsinized and counted after Trypan blue staining (Invitrogen) with a Hausser bright-line hemocytometer (Thermo Fisher Scientific). Annexin V/PI

staining was performed using the Dead Cell Apoptosis Kit (Thermo Fisher Scientific; V13245), according to the manufacturer's instructions. Staining was measured with a Becton Dickinson LSRFortessa flow cytometer and analyzed with FlowJo Version 10.2 software. Low-dilution-plating colony formation assays were performed by plating 1,000 cells in 12-well plates, followed by addition of THZ1 and/or other drugs the next day. Cells were fixed with 10% formalin 9–10 d after seeding and stained with crystal violet (0.05% solution) for 30 min. The plates were washed extensively and imaged with a flatbed scanner. For quantification, 1 ml methanol was added to each well to extract the dye, and absorbance was measured at 540 nm.

siRNA transfections

Cells were plated at 60% confluence in 6-well plates, and transient siRNA transfections (1 μ M) were performed using Lipofectamine 2000 (Invitrogen) and Opti-MEM (Invitrogen) according to the manufacturer's protocol (Zarei et al., 2017). 48 h after transfection, cells were treated or analyzed as described. siRNA oligonucleotides were purchased from Life Technologies (siCDK7, S2829; siCDK12, S28622; siCDK13, S16397; siNRF2, S9492; and siCTRL, AM4635).

Immunoblot analysis

Immunoblotting to detect protein detection was performed using SDS-PAGE as previously described (Lal et al., 2014). Membranes for immunoblotting were probed with antibodies against anti-phospho-CTD-RNAPII-S2 (04-1571; Millipore), anti-phospho-CTD-RNAPII-S5 (04-1572; Millipore), anti-CDK7 (2916; Cell Signaling Technology), anti-CDK13 (A301-458A; Bethyl), anti-cleaved poly(ADP ribose) polymerase (Asp214; 9541; Cell Signaling Technology), anti-cleaved caspase 3 (Asp175; 9664; Cell Signaling Technology), NRF2 (12721; Cell Signaling Technology), and anti- α -tubulin (Sigma-Aldrich). Chemiluminescent (32106; Thermo Fisher Scientific) signal was captured using a Syngene G-BOX iChemi XT imager.

Cellular ROS analysis

Cellular ROS levels were determined using 2',7'-dichlorodihydrofluorescein diacetate (DCFDA; Invitrogen). 5,000 cells/well were seeded in 96-well plates. 16 h later, 100 μ l phenol red-free DMEM containing 50 μ M DCFDA was added to each well. Fluorescence was measured using an excitation wavelength of 485 nm and emission wavelength of 535 nm on a BioTek Synergy HT plate reader.

Metabolomic profiling

Cells were grown to ~50% confluence in complete growth medium in 6-well plates in biological triplicates. The following day, cells were treated with THZ1 or other agents and incubated for 6 h. After rinses with HBSS, metabolites were extracted with 80% methanol and analyzed by targeted gas chromatography-MS via selected reaction monitoring, with polarity switching on a 5500 QTRAP triple quadrupole mass spectrometer (AB/SCIEX) coupled to a Prominence UFLC HPLC system (Shimadzu) using amide hydrophilic interaction liquid chromatography (Waters) at pH 9.2, as previously described (Metallo et al., 2011). 259

endogenous water-soluble metabolites were measured at steady state. The results were processed and analyzed using MetaboAnalyst 2.0.

MitoSOX staining for live cell imaging

MitoSOX Red mitochondrial superoxide indicator (M36008; Invitrogen) was used to localize intracellular ROS following the manufacturer's instructions. 5,000 cells grown in 6-well plates were treated with drugs or vehicle for 16 h, and then incubated with 5 μ M MitoSOX. After 10 min, the medium was removed, cells were rinsed with 1 \times PBS and counterstained for MitoTracker Green (M7514; Invitrogen), and ROS localization was visualized on a Zeiss LSM-510 Confocal Laser Microscope. MitoSOX Red fluorescence was measured at an excitation of 510 nm and emission of 580 nm using a BioTek Synergy HT plate reader.

ChIP sequencing (ChIP-seq) analysis of angiomyolipoma

50–100 mg pulverized tissue from frozen angiomyolipoma tumors was subjected to fixation for 10 min with 1% formaldehyde in 1 ml of 1 \times PBS (pH 7.4; Gibco; 10010-023), followed by 10-min quenching with 50 μ l of 0.125 M glycine. The fixed cells were rinsed twice with cold 1 \times PBS complete (1 \times PBS, 1 \times protease inhibitor cocktail, and 5 mM sodium butyrate), then they were spun down at 14,000 *g* for 30 s and the supernatant was aspirated. Frozen cross-linked cells were either stored at -80°C or were processed immediately.

Cross-linked cells were lysed with lysis buffer (0.1% SDS plus 1 \times TX-100, 10 mM Tris-HCl, pH 8, 1 mM EDTA, pH 8, 0.1% sodium deoxycholate, 0.25% sarkosyl, and 0.3 mM NaCl) and were sonicated in 1 ml milliTUBE using a Covaris E210 machine. Fixed cells from angiomyolipoma tumors were sonicated for 10 min per sample (sonication conditions: 5% duty; peak incident power 100; cycle, 200 cycles/burst).

After sonication, insoluble fragments were pelleted at 14,000 *g*, and a fraction of material (10–50 μ l) was subject to DNA isolation by treatment with 1 μ l of 10 mg/ml RNase (Roche; 11579681001) for 30 min at 37°C , addition of 5 μ l of 20 mg/ml Proteinase K (Roche; 3115879) for 6–16 h at 65°C , and purification using a PCR Purification kit (Qiagen; 28104). This purified sheared DNA was subjected to Agilent Bioanalyzer analysis (Agilent Technologies; 5067-4626) to confirm that DNA had been fragmented down to a size of 200–1,000 nt.

5 mg of sheared chromatin was incubated with 1 μ l of H3K27ac antibody (Sigma-Aldrich; C15410196) in protein G agarose bead columns with rotation at 4°C overnight. The beads were washed six times with 900 μ l of cold radioimmunoprecipitation assay buffer (50 mM Hepes, pH 7.6, 1 mM EDTA, 0.7% sodium deoxycholate, 1% NP-40, 0.5 M LiCl), and bound protein and cross-linked DNA were eluted in prewarmed 100- μ l elution buffer (1% SDS/0.1 M NaCO_3 in distilled H_2O). DNA was isolated from the immunoprecipitate as above. Libraries for sequencing were generated using the Rubicon ThruPLEX DNA-seq Quick Protocol (Takara Bio USA; R400406) and sequenced on the HiSeq 2500 instrument, with a median of 25 million reads obtained per sample. ROSE analysis for superenhancer calling was performed using the default parameters in Python 2.7.3, R 2.15.3,

and SAMtools 0.1.18 (http://younglab.wi.mit.edu/super_enhancer_code.html) as described (Lovén et al., 2013; Whyte et al., 2013).

Mouse studies

All experiments involving mice were approved by the Brigham and Women's Hospital Institutional Animal Care and Use Committee. 6-wk-old, female, athymic nude mice (Nude-Foxn1nu) were purchased from Harlan Laboratories (6903M). HCV.29 cells, or genetically modified variants of that cell line, were prepared in 100 μ l solution comprised of 70% Dulbecco's PBS and 30% Matrigel. Suspensions of 3×10^6 cells were then injected subcutaneously into the left and right flanks of mice. Tumor volumes were measured three times per wk using calipers (volume = length \times width²/2), along with body weight. Mice with established tumors (after 28 d, mean tumor volume of ~ 100 mm³) were randomly divided into four groups, which were then treated with vehicle (10% DMSO in PBS); THZ1 (3 mg/ml, prepared in vehicle solution, 10 mg/kg i.p. twice daily); rapamycin (3 mg/kg i.p. Monday, Wednesday, and Friday; LC Laboratories; R-5000); or a combination of both. Tumor volume was measured every 2–3 d. Upon harvesting, tumors were cut in half, with one half fixed in formalin overnight and then in 70% ethanol for histopathology analysis, and the other half snap frozen in liquid nitrogen for preparation of lysates.

Tsc2^{+/-} mice on the A/J background were described previously (Woodrum et al., 2010; Auricchio et al., 2012; Guo and Kwiatkowski, 2013). I.p. injections of vehicle, THZ1 (10 mg/kg twice daily), or rapamycin (3 mg/kg Monday, Wednesday, and Friday) were administered to female (five mice/treatment group) mice beginning at 5.5 mo of age. Mice were treated until day 30, when kidneys were harvested 10 h after the final treatment, fixed in formalin overnight, cut into 1-mm-wide sections, and embedded in paraffin. Following H&E staining, tumor volume measurements were made by two observers (H. Du and D.J. Kwiatkowski) blinded to treatment status, as described previously (Auricchio et al., 2012; Guo and Kwiatkowski, 2013). The total tumor volume per kidney was equal to sum of the tumor volume of each lesion identified, with tumor volume for each cyst/adenoma calculated as percent cellularity multiplied by cyst volume (tumor volume = maximum [percent lesion cellularity, 5%] $\times \pi/6 \times 1.64 \times$ [tumor length \times tumor width] $\times 1.5$).

RNA-seq

RNA-seq was performed on HCV.29.TSC1⁻ and HCV.29.TSC1⁺ cells. Cells were plated in 100-mm³ dishes in triplicate and treated with DMSO or 30 nM THZ1 for 6 h. Total RNA was extracted using the RNeasy mini kit (Qiagen) and analyzed on an Agilent 2100 Bioanalyzer for integrity. RNA-seq libraries were constructed by standard methods; 2 \times 75-bp paired-end reads and ~ 50 million reads were generated for each sample. Quality trimming on raw reads was performed using Cutadapt before sequence mapping (Martin, 2011). Sequence reads were aligned to the hg19 human genome build using the STAR aligning program (Dobin et al., 2013). A two-pass alignment was performed, and only those reads mapping uniquely to the human genome

were maintained for further analysis. Quantification of all genes and their isoforms was performed using fragments per kilobase of transcript per million mapped reads normalized values using Cufflinks v2.2.1; differentially expressed genes were identified using the DESeq2 package and manual analysis (Love et al., 2014). Expression levels for the HCV.29.TSC1⁻ and HCV.29.TSC1⁺, treated with control or two doses (30 nM and 100 nM) THZ1, were measured in duplicate. Raw data are provided in Table S4.

IHC

IHC staining was performed on paraffin-embedded tissue sections. Sections were incubated in three washes of Histo-clear (National Diagnostics; HS-200) for 5 min each, followed by two washes in 100% ethanol and two washes in 95% ethanol for 10 min each, then two washes in double-distilled H₂O (ddH₂O) for 5 min each. Antigen retrieval was performed by boiling for 10 min in 10 mM sodium citrate, pH 6.0, followed by washing in ddH₂O, then 3% hydrogen peroxide for 10 min, then ddH₂O again. 1 \times Tris-buffered saline and 0.1% Tween 20 (TBST) and 5% normal goat serum (Cell Signaling Technology; 5425) was used as a blocking solution for 1 h at room temperature. The following primary antibodies were diluted in Signal Stain Antibody Diluent (Cell Signaling Technology; 8112) and incubated overnight at 4°C: Ki67 (Abcam; ab16667), NRF2 (Cell Signaling Technology; 12721), and pS6^{S240/244} (Cell Signaling Technology; 5364). Slides were washed three times for 5 min each in 1 \times TBST and incubated in Signal Stain Boost IHC Detection Reagent (Cell Signaling Technology; 8114) for 30 min at room temperature, followed by three 5-min washes in 1 \times TBST. Signal was detected using the AEC Peroxidase (HRP) Substrate Kit (Vector; SK-4200) according to the manufacturer's instructions. Slides were counterstained with hematoxylin (Sigma-Aldrich). Coverslips were mounted with Permout Mounting solution (Thermo Fisher Scientific). TUNEL staining was performed with the In Situ Apoptosis Detection Kit (Trevigen; 4810-30-K).

Statistical analysis

Data were expressed as mean \pm SEM of at least three independent experiments. An unpaired, two-tailed Student's *t* test was used to determine the differences between groups (*, *P* < 0.05; **, *P* < 0.01; ***, *P* < 0.001). ANOVA was used for the analysis of tumor measurements among treated groups.

Accession numbers

RNA-seq data are deposited in GEO under accession no. GSE135527.

Online supplemental material

Fig. S1 shows that CDK7 inhibition by THZ1 selectively inhibits the growth of TSC mutant cells. Fig. S2 indicates that loss of CDK7 impairs TSC-deficient cell growth and proliferation. Fig. S3 shows that selective decrease of GSH levels is required for loss of CDK7-induced death of TSC-deficient cells. Fig. S4 indicates that inhibition of CDK7 leads to significant reductions in GSH synthetic gene expression in TSC mutant cells. Fig. S5 shows the effect CDK7 inhibition on the growth of TSC mutant

tumors. Table S1 lists cell lines used in this study. Table S2 contains the metabolomic data for 621.101, HCV.29, and MEF cell lines, under control conditions and after treatment with 30 nM THZ1. Table S3 contains metabolomic data for HCV.29 CDK7-KO and CTRL-KO cell lines, both control (TSC1⁻) and TSC1-intact (TSC1⁺). Table S4 contains cuff-count values for all genes determined through RNA-seq of HCV.29 cell lines before and after treatment with THZ1. Table S5 contains gene set enrichment analysis in THZ1-treated HCV.29.TSC1⁻ in comparison to THZ1-treated HCV.29.TSC1⁺. Table S6 contains RNA-seq analysis of NRF2 and NRF2-regulated GSH biosynthetic enzyme genes in HCV.29 cell lines after treatment with THZ1. Table S7 contains the clinical profile of angiomyolipoma patients.

Acknowledgments

This work was supported by the Engles Fund for TSC and LAM, the University of Pennsylvania Orphan Disease Center in partnership with the LAM Foundation, the US Department of Defense (DOD-W81XWH-18-1-0592 to M. Zarei; DOD-17-1-0205 to K. Giannikou), and the National Institutes of Health National Cancer Institute (IP01CA120964 to D.J. Kwiatkowski).

The authors declare no competing financial interests.

Author contributions: Study supervision, M. Zarei and D.J. Kwiatkowski; study concept and design, M. Zarei and D.J. Kwiatkowski; acquisition of data, M. Zarei, H. Du, A.H. Nassar, R.E. Yan, K. Giannikou, S.H. Johnson, H.C. Lam., J. Asara, and D.J. Kwiatkowski; analysis and interpretation of data, M. Zarei, H. Du, Y. Wang, T. Zhang, E.P. Henske, J. Asara, and D.J. Kwiatkowski; drafting of the manuscript, M. Zarei and D.J. Kwiatkowski; critical revision of the manuscript for important intellectual content: all authors.

Submitted: 7 February 2019

Revised: 26 June 2019

Accepted: 9 August 2019

References

- Akhtar, M.S., M. Heidemann, J.R. Tietjen, D.W. Zhang, R.D. Chapman, D. Eick, and A.Z. Ansari. 2009. TFIIH kinase places bivalent marks on the carboxy-terminal domain of RNA polymerase II. *Mol. Cell.* 34:387–393. <https://doi.org/10.1016/j.molcel.2009.04.016>
- Auricchio, N., I. Malinowska, R. Shaw, B.D. Manning, and D.J. Kwiatkowski. 2012. Therapeutic trial of metformin and bortezomib in a mouse model of tuberous sclerosis complex (TSC). *PLoS One.* 7:e31900. <https://doi.org/10.1371/journal.pone.0031900>
- Ben-Sahra, I., J.J. Howell, J.M. Asara, and B.D. Manning. 2013. Stimulation of de novo pyrimidine synthesis by growth signaling through mTOR and S6K1. *Science.* 339:1323–1328. <https://doi.org/10.1126/science.1228792>
- Ben-Sahra, I., G. Hoxhaj, S.J.H. Ricoult, J.M. Asara, and B.D. Manning. 2016. mTORC1 induces purine synthesis through control of the mitochondrial tetrahydrofolate cycle. *Science.* 351:728–733. <https://doi.org/10.1126/science.aad0489>
- Bissler, J.J., F.X. McCormack, L.R. Young, J.M. Elwing, G. Chuck, J.M. Leonard, V.J. Schmithorst, T. Laor, A.S. Brody, J. Bean, et al. 2008. Sirolimus for angiomyolipoma in tuberous sclerosis complex or lymphangioleiomyomatosis. *N. Engl. J. Med.* 358:140–151. <https://doi.org/10.1056/NEJMoa063564>
- Bissler, J.J., J.C. Kingswood, E. Radzikowska, B.A. Zonnenberg, M. Frost, E. Belousova, M. Sauter, N. Nonomura, S. Brakemeier, P.J. de Vries, et al. 2013. Everolimus for angiomyolipoma associated with tuberous sclerosis complex or sporadic lymphangioleiomyomatosis (EXIST-2): a multicentre, randomised, double-blind, placebo-controlled trial. *Lancet.* 381:817–824. [https://doi.org/10.1016/S0140-6736\(12\)61767-X](https://doi.org/10.1016/S0140-6736(12)61767-X)
- Bissler, J.J., J.C. Kingswood, E. Radzikowska, B.A. Zonnenberg, E. Belousova, M.D. Frost, M. Sauter, S. Brakemeier, P.J. de Vries, N. Berkowitz, et al. 2017. Everolimus long-term use in patients with tuberous sclerosis complex: Four-year update of the EXIST-2 study. *PLoS One.* 12: e0180939. <https://doi.org/10.1371/journal.pone.0180939>
- Brugarolas, J.B., F. Vazquez, A. Reddy, W.R. Sellers, and W.G. Kaelin Jr. 2003. TSC2 regulates VEGF through mTOR-dependent and -independent pathways. *Cancer Cell.* 4:147–158. [https://doi.org/10.1016/S1535-6108\(03\)00187-9](https://doi.org/10.1016/S1535-6108(03)00187-9)
- Chen, C., Y. Liu, R. Liu, T. Ikenoue, K.L. Guan, Y. Liu, and P. Zheng. 2008. TSC-mTOR maintains quiescence and function of hematopoietic stem cells by repressing mitochondrial biogenesis and reactive oxygen species. *J. Exp. Med.* 205:2397–2408. <https://doi.org/10.1084/jem.20081297>
- Chio, I.L.C., and D.A. Tuveson. 2017. ROS in Cancer: The Burning Question. *Trends Mol. Med.* 23:411–429. <https://doi.org/10.1016/j.molmed.2017.03.004>
- Chipmuro, E., E. Marco, C.L. Christensen, N. Kwiatkowski, T. Zhang, C.M. Hatheway, B.J. Abraham, B. Sharma, C. Yeung, A. Altabel, et al. 2014. CDK7 inhibition suppresses super-enhancer-linked oncogenic transcription in MYCN-driven cancer. *Cell.* 159:1126–1139. <https://doi.org/10.1016/j.cell.2014.10.024>
- Choo, A.Y., S.G. Kim, M.G. Vander Heiden, S.J. Mahoney, H. Vu, S.O. Yoon, L.C. Cantley, and J. Blenis. 2010. Glucose addition of TSC null cells is caused by failed mTORC1-dependent balancing of metabolic demand with supply. *Mol. Cell.* 38:487–499. <https://doi.org/10.1016/j.molcel.2010.05.007>
- Christensen, C.L., N. Kwiatkowski, B.J. Abraham, J. Carretero, F. Al-Shahrour, T. Zhang, E. Chipmuro, G.S. Herter-Sprie, E.A. Akbay, A. Altabel, et al. 2014. Targeting transcriptional additions in small cell lung cancer with a covalent CDK7 inhibitor. *Cancer Cell.* 26:909–922. <https://doi.org/10.1016/j.ccr.2014.10.019>
- Crino, P.B., K.L. Nathanson, and E.P. Henske. 2006. The tuberous sclerosis complex. *N. Engl. J. Med.* 355:1345–1356. <https://doi.org/10.1056/NEJMra055323>
- Davies, M., A. Saxena, and J.C. Kingswood. 2017. Management of everolimus-associated adverse events in patients with tuberous sclerosis complex: a practical guide. *Orphanet J. Rare Dis.* 12:35. <https://doi.org/10.1186/s13023-017-0581-9>
- Dibble, C.C., W. Elis, S. Menon, W. Qin, J. Klekota, J.M. Asara, P.M. Finan, D.J. Kwiatkowski, L.O. Murphy, and B.D. Manning. 2012. TBC1D7 is a third subunit of the TSC1-TSC2 complex upstream of mTORC1. *Mol. Cell.* 47: 535–546. <https://doi.org/10.1016/j.molcel.2012.06.009>
- Dickson, M.A., G.K. Schwartz, C.R. Antonescu, D.J. Kwiatkowski, and I.A. Malinowska. 2013. Extrarenal perivascular epithelioid cell tumors (PEComas) respond to mTOR inhibition: clinical and molecular correlates. *Int. J. Cancer.* 132:1711–1717. <https://doi.org/10.1002/ijc.27800>
- Dobin, A., C.A. Davis, F. Schlesinger, J. Drenkow, C. Zaleski, S. Jha, P. Batut, M. Chaisson, and T.R. Gingeras. 2013. STAR: ultrafast universal RNA-seq aligner. *Bioinformatics.* 29:15–21. <https://doi.org/10.1093/bioinformatics/bts635>
- Drapkin, R., G. Le Roy, H. Cho, S. Akoulitchiev, and D. Reinberg. 1996. Human cyclin-dependent kinase-activating kinase exists in three distinct complexes. *Proc. Natl. Acad. Sci. USA.* 93:6488–6493. <https://doi.org/10.1073/pnas.93.13.6488>
- Düvel, K., J.L. Yecies, S. Menon, P. Raman, A.I. Lipovsky, A.L. Souza, E. Triantafellow, Q. Ma, R. Gorski, S. Cleaver, et al. 2010. Activation of a metabolic gene regulatory network downstream of mTOR complex 1. *Mol. Cell.* 39:171–183. <https://doi.org/10.1016/j.molcel.2010.06.022>
- El-Hashemite, N., V. Walker, H. Zhang, and D.J. Kwiatkowski. 2003. Loss of Tsc1 or Tsc2 induces vascular endothelial growth factor production through mammalian target of rapamycin. *Cancer Res.* 63:5173–5177.
- European Chromosome 16 Tuberous Sclerosis Consortium. 1993. Identification and characterization of the tuberous sclerosis gene on chromosome 16. *Cell.* 75:1305–1315. [https://doi.org/10.1016/0092-8674\(93\)90618-Z](https://doi.org/10.1016/0092-8674(93)90618-Z)
- Finlay, G.A., D.S. Hunter, C.L. Walker, K.E. Paulson, and B.L. Fanburg. 2003. Regulation of PDGF production and ERK activation by estrogen is associated with TSC2 gene expression. *Am. J. Physiol. Cell Physiol.* 285: C409–C418. <https://doi.org/10.1152/ajpcell.00482.2002>
- Finlay, G.A., V.J. Thannickal, B.L. Fanburg, and D.J. Kwiatkowski. 2005. Platelet-derived growth factor-induced p42/44 mitogen-activated protein kinase activation and cellular growth is mediated by reactive oxygen species in the absence of TSC2/tuberin. *Cancer Res.* 65: 10881–10890. <https://doi.org/10.1158/0008-5472.CAN-05-1394>

- Franz, D.N., J. Leonard, C. Tudor, G. Chuck, M. Care, G. Sethuraman, A. Di-nopoulos, G. Thomas, and K.R. Crone. 2006. Rapamycin causes regression of astrocytomas in tuberous sclerosis complex. *Ann. Neurol.* 59: 490–498. <https://doi.org/10.1002/ana.20784>
- Franz, D.N., E. Belousova, S. Sparagana, E.M. Bebin, M. Frost, R. Kuperman, O. Witt, M.H. Kohrman, J.R. Flamini, J.Y. Wu, et al. 2013. Efficacy and safety of everolimus for subependymal giant cell astrocytomas associated with tuberous sclerosis complex (EXIST-1): a multicentre, randomised, placebo-controlled phase 3 trial. *Lancet.* 381:125–132. [https://doi.org/10.1016/S0140-6736\(12\)61134-9](https://doi.org/10.1016/S0140-6736(12)61134-9)
- Glover-Cutter, K., S. Larochelle, B. Erickson, C. Zhang, K. Shokat, R.P. Fisher, and D.L. Bentley. 2009. TFIIF-associated Cdk7 kinase functions in phosphorylation of C-terminal domain Ser7 residues, promoter-proximal pausing, and termination by RNA polymerase II. *Mol. Cell. Biol.* 29:5455–5464. <https://doi.org/10.1128/MCB.00637-09>
- Gorriani, C., I.S. Harris, and T.W. Mak. 2013. Modulation of oxidative stress as an anticancer strategy. *Nat. Rev. Drug Discov.* 12:931–947. <https://doi.org/10.1038/nrd4002>
- Grabner, B.C., V. Nardi, K. Birsoy, R. Possemato, K. Shen, S. Sinha, A. Jordan, A.H. Beck, and D.M. Sabatini. 2014. A diverse array of cancer-associated MTOR mutations are hyperactivating and can predict rapamycin sensitivity. *Cancer Discov.* 4:554–563. <https://doi.org/10.1158/2159-8290.CD-13-0929>
- Guo, Y., and D.J. Kwiatkowski. 2013. Equivalent benefit of rapamycin and a potent mTOR ATP-competitive inhibitor, MLN0128 (INK128), in a mouse model of tuberous sclerosis. *Mol. Cancer Res.* 11:467–473. <https://doi.org/10.1158/1541-7786.MCR-12-0605>
- Guo, Y., Y. Chekaluk, J. Zhang, J. Du, N.S. Gray, C.L. Wu, and D.J. Kwiatkowski. 2013. TSC1 involvement in bladder cancer: diverse effects and therapeutic implications. *J. Pathol.* 230:17–27. <https://doi.org/10.1002/path.4176>
- Hara, K., K. Yonezawa, Q.P. Weng, M.T. Kozlowski, C. Belham, and J. Avruch. 1998. Amino acid sufficiency and mTOR regulate p70 S6 kinase and eIF-4E BP1 through a common effector mechanism. *J. Biol. Chem.* 273: 14484–14494. <https://doi.org/10.1074/jbc.273.23.14484>
- Harvey, C.J., R.K. Thimmulappa, A. Singh, D.J. Blake, G. Ling, N. Watabayashi, J. Fujii, A. Myers, and S. Biswal. 2009. Nrf2-regulated glutathione recycling independent of biosynthesis is critical for cell survival during oxidative stress. *Free Radic. Biol. Med.* 46:443–453. <https://doi.org/10.1016/j.freeradbiomed.2008.10.040>
- Hayes, J.D., and A.T. Dinkova-Kostova. 2014. The Nrf2 regulatory network provides an interface between redox and intermediary metabolism. *Trends Biochem. Sci.* 39:199–218. <https://doi.org/10.1016/j.tibs.2014.02.002>
- Henske, E.P., S. Jóźwiak, J.C. Kingswood, J.R. Sampson, and E.A. Thiele. 2016. Tuberous sclerosis complex. *Nat. Rev. Dis. Primers.* 2:16035. <https://doi.org/10.1038/nrdp.2016.35>
- Huang, J., C.C. Dibble, M. Matsuzaki, and B.D. Manning. 2008. The TSC1-TSC2 complex is required for proper activation of mTOR complex 2. *Mol. Cell. Biol.* 28:4104–4115. <https://doi.org/10.1128/MCB.00289-08>
- Inoki, K., Y. Li, T. Xu, and K.L. Guan. 2003. Rheb GTPase is a direct target of TSC2 GAP activity and regulates mTOR signaling. *Genes Dev.* 17: 1829–1834. <https://doi.org/10.1101/gad.1110003>
- Kim, J.E., and J. Chen. 2004. regulation of peroxisome proliferator-activated receptor-gamma activity by mammalian target of rapamycin and amino acids in adipogenesis. *Diabetes.* 53:2748–2756. <https://doi.org/10.2337/diabetes.53.11.2748>
- Kim, J., J. Kim, and J.S. Bae. 2016. ROS homeostasis and metabolism: a critical liaison for cancer therapy. *Exp. Mol. Med.* 48:e269. <https://doi.org/10.1038/emmm.2016.119>
- Krueger, D.A., M.M. Care, K. Holland, K. Agricola, C. Tudor, P. Mangeskar, K.A. Wilson, A. Byars, T. Sahmoud, and D.N. Franz. 2010. Everolimus for subependymal giant-cell astrocytomas in tuberous sclerosis. *N. Engl. J. Med.* 363:1801–1811. <https://doi.org/10.1056/NEJMoa1001671>
- Kwiatkowski, N., T. Zhang, P.B. Rahl, B.J. Abraham, J. Reddy, S.B. Ficarro, A. Dastur, A. Amzallag, S. Ramaswamy, B. Tesar, et al. 2014. Targeting transcription regulation in cancer with a covalent CDK7 inhibitor. *Nature.* 511:616–620. <https://doi.org/10.1038/nature13393>
- Lal, S., R.A. Burkhart, N. Beehar, V. Bhattacharjee, E.R. Londin, J.A. Coz-zitorto, C. Romeo, M. Jimbo, Z.A. Norris, C.J. Yeo, et al. 2014. HuR posttranscriptionally regulates WEE1: implications for the DNA damage response in pancreatic cancer cells. *Cancer Res.* 74:1128–1140. <https://doi.org/10.1158/0008-5472.CAN-13-1915>
- Larochelle, S., R. Amat, K. Glover-Cutter, M. Sansó, C. Zhang, J.J. Allen, K.M. Shokat, D.L. Bentley, and R.P. Fisher. 2012. Cyclin-dependent kinase control of the initiation-to-elongation switch of RNA polymerase II. *Nat. Struct. Mol. Biol.* 19:1108–1115. <https://doi.org/10.1038/nsmb.2399>
- Li, C., P.S. Lee, Y. Sun, X. Gu, E. Zhang, Y. Guo, C.L. Wu, N. Auricchio, C. Priolo, J. Li, et al. 2014. Estradiol and mTORC2 cooperate to enhance prostaglandin biosynthesis and tumorigenesis in TSC2-deficient LAM cells. *J. Exp. Med.* 211:15–28. <https://doi.org/10.1084/jem.20131080>
- Li, J., A. Csibi, S. Yang, G.R. Hoffman, C. Li, E. Zhang, J.J. Yu, and J. Blenis. 2015. Synthetic lethality of combined glutaminase and Hsp90 inhibition in mTORC1-driven tumor cells. *Proc. Natl. Acad. Sci. USA.* 112:E21–E29. <https://doi.org/10.1073/pnas.1417015112>
- Li, S., M.S. Brown, and J.L. Goldstein. 2010. Bifurcation of insulin signaling pathway in rat liver: mTORC1 required for stimulation of lipogenesis, but not inhibition of gluconeogenesis. *Proc. Natl. Acad. Sci. USA.* 107: 3441–3446. <https://doi.org/10.1073/pnas.0914798107>
- Liou, G.Y., and P. Storz. 2010. Reactive oxygen species in cancer. *Free Radic. Res.* 44:479–496. <https://doi.org/10.3109/10715761003667554>
- Love, M.I., W. Huber, and S. Anders. 2014. Moderated estimation of fold change and dispersion for RNA-seq data with DESeq2. *Genome Biol.* 15: 550. <https://doi.org/10.1186/s13059-014-0550-8>
- Lovén, J., H.A. Hoke, C.Y. Lin, A. Lau, D.A. Orlando, C.R. Vakoc, J.E. Bradner, T.I. Lee, and R.A. Young. 2013. Selective inhibition of tumor oncogenes by disruption of super-enhancers. *Cell.* 153:320–334. <https://doi.org/10.1016/j.cell.2013.03.036>
- Martin, M. 2011. Cutadapt removes adapter sequences from high-throughput sequencing reads. *EMBnet.journal.* 17:10–12. <https://doi.org/10.14806/ej.17.1.200>
- McCormack, F.X., Y. Inoue, J. Moss, L.G. Singer, C. Strange, K. Nakata, A.F. Barker, J.T. Chapman, M.L. Brantly, J.M. Stocks, et al. MILES Trial Group. 2011. Efficacy and safety of sirolimus in lymphangioleiomyomatosis. *N. Engl. J. Med.* 364:1595–1606. <https://doi.org/10.1056/NEJMoa1100391>
- Metallo, C.M., P.A. Gameiro, E.L. Bell, K.R. Mattaini, J. Yang, K. Hiller, C.M. Jewell, Z.R. Johnson, D.J. Irvine, L. Guarente, et al. 2011. Reductive glutamine metabolism by IDH1 mediates lipogenesis under hypoxia. *Nature.* 481:380–384. <https://doi.org/10.1038/nature10602>
- Moloney, J.N., and T.G. Cotter. 2018. ROS signalling in the biology of cancer. *Semin. Cell Dev. Biol.* 80:50–64. <https://doi.org/10.1016/j.semcdb.2017.05.023>
- Onda, H., P.B. Crino, H. Zhang, R.D. Murphey, L. Rastelli, B.E. Gould Roth-berg, and D.J. Kwiatkowski. 2002. Tsc2 null murine neuroepithelial cells are a model for human tuber giant cells, and show activation of an mTOR pathway. *Mol. Cell. Neurosci.* 21:561–574. <https://doi.org/10.1006/mcne.2002.1184>
- Parkhitko, A.A., C. Priolo, J.L. Colloff, J. Yun, J.J. Wu, K. Mizumura, W. Xu, I.A. Malinowska, J. Yu, D.J. Kwiatkowski, et al. 2014. Autophagy-dependent metabolic reprogramming sensitizes TSC2-deficient cells to the anti-metabolite 6-aminonicotinamide. *Mol. Cancer Res.* 12:48–57. <https://doi.org/10.1158/1541-7786.MCR-13-0258-T>
- Ricketts, C.J., A.A. De Cubas, H. Fan, C.C. Smith, M. Lang, E. Reznik, R. Bowlby, E.A. Gibb, R. Akbani, R. Beroukhi, et al. Cancer Genome Atlas Research Network. 2018. The Cancer Genome Atlas Comprehensive Molecular Characterization of Renal Cell Carcinoma. *Cell Reports.* 23: 3698. <https://doi.org/10.1016/j.celrep.2018.06.032>
- Rimel, J.K., and D.J. Taatjes. 2018. The essential and multifunctional TFIIF complex. *Protein Sci.* 27:1018–1037. <https://doi.org/10.1002/pro.3424>
- Robertson, A.G., J. Kim, H. Al-Ahmadie, J. Bellmunt, G. Guo, A.D. Cherniack, T. Hinoue, P.W. Laird, K.A. Hoadley, R. Akbani, et al. TCGA Research Network. 2017. Comprehensive Molecular Characterization of Muscle-Invasive Bladder Cancer. *Cell.* 171:540–556.e25. <https://doi.org/10.1016/j.cell.2017.09.007>
- Settembre, C., R. Zoncu, D.L. Medina, F. Vetrini, S. Erdin, S. Erdin, T. Huynh, M. Ferron, G. Karsenty, M.C. Vellard, et al. 2012. A lysosome-to-nucleus signalling mechanism senses and regulates the lysosome via mTOR and TFEb. *EMBO J.* 31:1095–1108. <https://doi.org/10.1038/emboj.2012.32>
- Singh, A., S. Venkannagari, K.H. Oh, Y.Q. Zhang, J.M. Rohde, L. Liu, S. Nimmagadda, K. Sudini, K.R. Brimacombe, S. Gajghate, et al. 2016. Small Molecule Inhibitor of NRF2 Selectively Intervenes Therapeutic Resistance in KEAP1-Deficient NSCLC Tumors. *ACS Chem. Biol.* 11: 3214–3225. <https://doi.org/10.1021/acscchembio.6b00651>
- Teppo, H.R., Y. Soini, and P. Karihtala. 2017. Reactive Oxygen Species-Mediated Mechanisms of Action of Targeted Cancer Therapy. *Oxid. Med. Cell. Longev.* 2017:1485283. <https://doi.org/10.1155/2017/1485283>
- Tonelli, C., I.L.C. Chio, and D.A. Tuveson. 2018. Transcriptional Regulation by Nrf2. *Antioxid. Redox Signal.* 29:1727–1745. <https://doi.org/10.1089/ars.2017.7342>
- Trachootham, D., J. Alexandre, and P. Huang. 2009. Targeting cancer cells by ROS-mediated mechanisms: a radical therapeutic approach? *Nat. Rev. Drug Discov.* 8:579–591. <https://doi.org/10.1038/nrd2803>

- Valvezan, A.J., M. Turner, A. Belaid, H.C. Lam, S.K. Miller, M.C. McNamara, C. Baglini, B.E. Housden, N. Perrimon, D.J. Kwiatkowski, et al. 2017. mTORC1 Couples Nucleotide Synthesis to Nucleotide Demand Resulting in a Targetable Metabolic Vulnerability. *Cancer Cell*. 32:624–638.e5. <https://doi.org/10.1016/j.ccell.2017.09.013>
- van Slegtenhorst, M., R. de Hoogt, C. Hermans, M. Nellist, B. Janssen, S. Verhoef, D. Lindhout, A. van den Ouweland, D. Halley, J. Young, et al. 1997. Identification of the tuberous sclerosis gene TSC1 on chromosome 9q34. *Science*. 277:805–808. <https://doi.org/10.1126/science.277.5327.805>
- Venditti, P., L. Di Stefano, and S. Di Meo. 2013. Mitochondrial metabolism of reactive oxygen species. *Mitochondrion*. 13:71–82. <https://doi.org/10.1016/j.mito.2013.01.008>
- Wang, B.T., G.S. Ducker, A.J. Barczak, R. Barbeau, D.J. Erle, and K.M. Shokat. 2011. The mammalian target of rapamycin regulates cholesterol biosynthetic gene expression and exhibits a rapamycin-resistant transcriptional profile. *Proc. Natl. Acad. Sci. USA*. 108:15201–15206. <https://doi.org/10.1073/pnas.1103746108>
- Wang, Y., T. Zhang, N. Kwiatkowski, B.J. Abraham, T.I. Lee, S. Xie, H. Yuzugullu, T. Von, H. Li, Z. Lin, et al. 2015. CDK7-dependent transcriptional addiction in triple-negative breast cancer. *Cell*. 163:174–186. <https://doi.org/10.1016/j.cell.2015.08.063>
- Whyte, W.A., D.A. Orlando, D. Hnisz, B.J. Abraham, C.Y. Lin, M.H. Kagey, P.B. Rahl, T.I. Lee, and R.A. Young. 2013. Master transcription factors and mediator establish super-enhancers at key cell identity genes. *Cell*. 153:307–319. <https://doi.org/10.1016/j.cell.2013.03.035>
- Woodrum, C., A. Nabil, and S.L. Dabora. 2010. Comparison of three rapamycin dosing schedules in A/J Tsc2[±] mice and improved survival with angiogenesis inhibitor or asparaginase treatment in mice with subcutaneous tuberous sclerosis related tumors. *J. Transl. Med.* 8:14. <https://doi.org/10.1186/1479-5876-8-14>
- Yecies, J.L., H.H. Zhang, S. Menon, S. Liu, D. Yecies, A.I. Lipovsky, C. Gorgun, D.J. Kwiatkowski, G.S. Hotamisligil, C.H. Lee, and B.D. Manning. 2011. Akt stimulates hepatic SREBP1c and lipogenesis through parallel mTORC1-dependent and independent pathways. *Cell Metab.* 14:21–32. <https://doi.org/10.1016/j.cmet.2011.06.002>
- Yokogami, K., S. Wakisaka, J. Avruch, and S.A. Reeves. 2000. Serine phosphorylation and maximal activation of STAT3 during CNTF signaling is mediated by the rapamycin target mTOR. *Curr. Biol.* 10:47–50. [https://doi.org/10.1016/S0960-9822\(99\)00268-7](https://doi.org/10.1016/S0960-9822(99)00268-7)
- Yu, J., A. Astrinidis, S. Howard, and E.P. Henske. 2004. Estradiol and tamoxifen stimulate LAM-associated angiomylipoma cell growth and activate both genomic and nongenomic signaling pathways. *Am. J. Physiol. Lung Cell. Mol. Physiol.* 286:L694–L700. <https://doi.org/10.1152/ajplung.00204.2003>
- Zarei, M., S. Lal, S.J. Parker, A. Nevler, A. Vaziri-Gohar, K. Dukleska, N.C. Mambelli-Lisboa, C. Moffat, F.F. Blanco, S.N. Chand, et al. 2017. Post-transcriptional Upregulation of IDH1 by HuR Establishes a Powerful Survival Phenotype in Pancreatic Cancer Cells. *Cancer Res.* 77:4460–4471. <https://doi.org/10.1158/0008-5473.CAN-17-0015>
- Zhang, H., G. Cicchetti, H. Onda, H.B. Koon, K. Asrican, N. Bajraszewski, F. Vazquez, C.L. Carpenter, and D.J. Kwiatkowski. 2003. Loss of Tsc1/Tsc2 activates mTOR and disrupts PI3K-Akt signaling through down-regulation of PDGFR. *J. Clin. Invest.* 112:1223–1233. <https://doi.org/10.1172/JCI200317222>
- Zhang, Y., J. Nicholatos, J.R. Dreier, S.J. Ricoult, S.B. Widenmaier, G.S. Hotamisligil, D.J. Kwiatkowski, and B.D. Manning. 2014. Coordinated regulation of protein synthesis and degradation by mTORC1. *Nature*. 513:440–443. <https://doi.org/10.1038/nature13492>
- Zhang, Z., H. Peng, X. Wang, X. Yin, P. Ma, Y. Jing, M.C. Cai, J. Liu, M. Zhang, S. Zhang, et al. 2017. Preclinical Efficacy and Molecular Mechanism of Targeting CDK7-Dependent Transcriptional Addiction in Ovarian Cancer. *Mol. Cancer Ther.* 16:1739–1750. <https://doi.org/10.1158/1535-7163.MCT-17-0078>
- Zhou, Q., T. Li, and D.H. Price. 2012. RNA polymerase II elongation control. *Annu. Rev. Biochem.* 81:119–143. <https://doi.org/10.1146/annurev-biochem-052610-095910>